



HAL
open science

Geothermal Modeling in Complex Geological Systems with ComPASS

Antoine Armandine Les Landes, Laurence Beau de, Daniel Castanon Quiroz,
Laurent Jeannin, Simon Lopez, Farid Smaï, Théophile Guillon, Roland
Masson

► **To cite this version:**

Antoine Armandine Les Landes, Laurence Beau de, Daniel Castanon Quiroz, Laurent Jeannin, Simon Lopez, et al.. Geothermal Modeling in Complex Geological Systems with ComPASS. 2023. hal-04246471

HAL Id: hal-04246471

<https://brgm.hal.science/hal-04246471>

Preprint submitted on 17 Oct 2023

HAL is a multi-disciplinary open access archive for the deposit and dissemination of scientific research documents, whether they are published or not. The documents may come from teaching and research institutions in France or abroad, or from public or private research centers.

L'archive ouverte pluridisciplinaire **HAL**, est destinée au dépôt et à la diffusion de documents scientifiques de niveau recherche, publiés ou non, émanant des établissements d'enseignement et de recherche français ou étrangers, des laboratoires publics ou privés.

```

1
2 File: main_document.tex
3 Encoding: utf8
4 Sum count: 6441
5 Words in text: 5869
6 Words in headers: 99
7 Words outside text (captions, etc.): 324
8 Number of headers: 32
9 Number of floats/tables/figures: 19
10 Number of math inlines: 140
11 Number of math displayed: 9
12 Subcounts:
13   text+headers+captions (#headers/#floats/#inlines/#displayed)
14   204+8+0 (1/0/0/0) _top_
15   1041+1+0 (1/0/1/0) Section: Introduction
16   42+2+0 (1/0/0/0) Section: Model description
17   351+10+0 (3/0/45/9) Subsection: Multi-phase multi-component model
18   590+11+0 (3/0/0/0) Subsection: Hybrid model with lower dimension elements
19   234+2+62 (1/2/26/0) Subsection: Spatial discretization}\label{sec:spatial_discretization
20   1124+10+0 (5/0/5/0) Subsection: Numerical aspects
21   106+2+0 (1/0/1/0) Section: Case studies
22   1136+27+135 (7/8/36/0) Subsection: Liquid dominated reservoir
23   487+16+127 (5/9/26/0) Subsection: Steam-dominated reservoir
24   349+3+0 (1/0/0/0) Section: Conclusions and perspectives
25   66+1+0 (1/0/0/0) Section: Acknowledgments
26   113+2+0 (1/0/0/0) Section: Code availability
27   26+4+0 (1/0/0/0) Section: Declaration of Competing Interest
28
29
30 (errors:1)

```

31 Cover Letter

32 **Geothermal Modeling in Complex Geological Systems with ComPASS**

33 A. Armandine Les Landes, L. Beaudé, D. Castanon Quiroz, L. Jeannin, S. Lopez, F. Smai, T. Guillon, R. Masson

34 Dear Editors-in-Chief,

35
36 Please find the enclosed manuscript "Geothermal Modeling in Complex Geological Systems with ComPASS" which
37 we are submitting for exclusive consideration for publication in Computers & Geosciences. The submission fulfills all
38 the necessary requirements and includes all items listed in the submission checklist.

39
40 Following an issue detected during the pre-review phase (significant amount of textual overlap with previously pub-
41 lished works). The manuscript has been updated to limit the number of literal correspondences with previous works.
42 However, we want to clarify that most of the identified literal correspondences were legitimate. Indeed, the majority
43 of these correspondences are consistent with the code's description, which was published in parts as it was completed.
44 The authors of this manuscript (Lopez, Masson, Beaudé, Castanon Quiroz, Smai) contributed to the development of
45 the code described in these earlier publications and communications. Finally, in response to the request, sub-sections
46 have been added to segment bulky parts of the manuscript and the paper has been shortened.

47
48 In the manuscript, we introduce the ComPASS geothermal flow simulator with its improvements and demonstrate its
49 practical application in field-scale geothermal reservoir models.

50
51 The computer source codes are made available to the public in a repository, and the relevant information can be found
52 in the "Computer Code availability" section. Scripts and meshes to reproduce the simulation results for each test case
53 presented in this article are provided in the public repository, as mentioned in the code availability section.

54 Thanks for your consideration.

55
56 Sincerely,

57
58 A. Armandine Les Landes, L. Beaudé, D. Castanon Quiroz, L. Jeannin, S. Lopez, F. Smai, T. Guillon and R. Masson

59
60 A. Armandine Les Landes, BRGM, 3 avenue Claude-Guillemin, BP 36009, 45060 Orléans Cedex 2, France,

61 A.ArmandineLesLandes@brgm.fr

62

63 Highlights

64 **Geothermal Modeling in Complex Geological Systems with ComPASS**

65 A. Armandine Les Landes, L. Beaudé, D. Castanon Quiroz, L. Jeannin, S. Lopez, F. Smay, T. Guillon, R. Masson

- 66 • ComPASS is an open-source, evolutive, massively parallel platform for hydrothermal modeling.
- 67 • ComPASS core is written in compiled high-performance and a Python API allows simulation setup.
- 68 • ComPASS uses compact finite volume scheme for multi-phase Darcy flow on unstructured meshes.
- 69 • Unstructured meshes enable modeling of complex geometry like faults, fractures, and deviated wells in Com-
70 PASS.
- 71 • ComPASS uses non-isothermal Coats formulation to solve multi-phase, multi-component Darcy flows.
- 72 • ComPASS models large and complex geothermal reservoirs effectively.
- 73 • ComPASS simulations prove effective for highly non-linear, large-scale problems.

74 Geothermal Modeling in Complex Geological Systems with 75 ComPASS

76 A. Armandine Les Landes^a, L. Beaude^b, D. Castanon Quiroz^c, L. Jeannin^d, S. Lopez^e,
77 F. Smai^f, T. Guillon^g and R. Masson^h

78 ^aBRGM, 3 avenue Claude-Guillemin, BP 36009, 45060 Orléans Cedex 2, France, a.armandineLesLandes@brgm.fr

79 ^bBRGM, 3 avenue Claude-Guillemin, BP 36009, 45060 Orléans Cedex 2, France, l.beaude@brgm.fr

80 ^c Instituto de Investigaciones en Matemáticas Aplicadas y en Sistemas, Universidad Nacional Autónoma de México, Circuito Escolar s/n, Ciudad
81 Universitaria C.P. 04510 Cd. Mx. (México), daniel.castanon@iimas.unam.mx

82 ^dSTORENGY, 12 rue Raoul Nordling - Djinn - CS 70001 92274 Bois Colombes Cedex, France, laurent.jeannin@storengy.com

83 ^eBRGM, 3 avenue Claude-Guillemin, BP 36009, 45060 Orléans Cedex 2, France, s.lopez@brgm.fr

84 ^fBRGM, 3 avenue Claude-Guillemin, BP 36009, 45060 Orléans Cedex 2, France, f.smai@brgm.fr

85 ^gBRGM, 3 avenue Claude-Guillemin, BP 36009, 45060 Orléans Cedex 2, France, t.guillon@brgm.fr

86 ^hUniversité Côte d'Azur, Inria, CNRS, LJAD, UMR 7351 CNRS, team Coffee, Parc Valrose 06108 Nice Cedex 02, France,

87 roland.masson@univ-cotedazur.fr

90 ARTICLE INFO

92 Keywords:

93 geothermal reservoir modeling
94 multi-component multi-phase flow
95 unstructured meshes
96 faulted and fractured reservoir
97 deviated wells

90 ABSTRACT

In deep geothermal reservoirs, faults and fractures play a major role, serving as regulators of fluid flow and heat transfer while also providing feed zones for production wells. To accurately model the operation of geothermal fields, it is necessary to explicitly consider objects of varying spatial scales, from the reservoir scale itself, to that of faults and fractures, down to the scale of the injection and production wells.

Our main objective in developing the ComPASS geothermal flow simulator, was to take into account all of these geometric constraints in a flow and heat transfer numerical model using generic unstructured meshes. In its current state, the code provides a parallel implementation of a spatio-temporal discretization of the non-linear equations driving compositional multi-phase thermal flows in porous fractured media on unstructured meshes. It allows an explicit discretization of faults and fractures as 2D hybrid objects, embedded in a 3D matrix. Similarly, wells are modeled as one dimensional graphs discretized by edges of the 3D mesh which allows arbitrary multi-branch wells. The resulting approach is particularly flexible and robust in terms of modeling.

Its practical interest is demonstrated by two case studies in high-energy geothermal contexts.

108 CRedit authorship contribution statement

109 **A. Armandine Les Landes:** Simulations, case studies, Visualization, meshing, Writing. **L. Beaude:** Model
110 description, code developer, Writing - review and editing. **D. Castanon Quiroz:** Well model development, Writing
111 - review and editing. **L. Jeannin:** Interpretation of the results, Supervision, Writing - review and editing. **S. Lopez:**
112 Model description, Supervision, code developer, Interpretation of the results, Writing - review and editing. **F. Smai:**
113 code developer. **T. Guillon:** code developer - meshing. **R. Masson:** Developed the theoretical formalism and early
114 versions of the code, Writing - review and editing.

115 1. Introduction

116 Geothermal resources are already widely available in areas with volcanic activity and in sedimentary basins and
117 their exploitation could significantly contribute to the decarbonization of our economy (Hirschberg et al., 2014). In
118 contrast to other renewable energy sources, geothermal energy is weather-independent and can provide both electric-
119 ity and heat, as well as value-added mineral extraction. Geothermal power production provides reliable generation

ORCID(s): 0000-0000-0000-0000 (A.A.L. Landes)

120 with high plant efficiency, low greenhouse gas emissions and a small ecological footprint. Moreover, it is usually a
121 long-lasting sustainable source when properly managed (International Renewable Energy Agency and International
122 Geothermal Association, 2023).

123 Numerical modeling has been one of the cornerstones of such management for decades and has become an es-
124 sential tool at all stages of exploration and development of geothermal projects (O’Sullivan et al., 2001; O’Sullivan
125 and O’Sullivan, 2016; Nugraha et al., 2022). The usual starting point is a conceptual model that often relies on 3D
126 geological modeling capabilities. Then, flow modeling is used during the exploration phases to understand the natural
127 resource, to evaluate the geothermal potential, to validate conceptual hypotheses, and on the other hand, during the
128 development of geothermal assets to predict production flow rates (*e.g.* among many others: Ingebritsen et al. (2010);
129 Daniilidis et al. (2021); Jalilinasrabady et al. (2021); O’Sullivan et al. (2009); O’Sullivan and O’Sullivan (2016); Nu-
130 graha et al. (2022)...). Not only do the models provide a coherent vision of the geothermal system by integrating all the
131 data and measurements, but above all they represent a quantitative tool for decision making and planning production
132 and development of the resource.

133 By many aspects, integrating multi-disciplinary contributions in a shared consistent numerical model of the subsur-
134 face remains a complex but worthwhile challenge to mitigate risks (Lopez et al., 2017). Passing from a 3D geological
135 model to an hydrothermal numerical model while preserving realistic geometries in flow simulations is a crucial step
136 of the geothermal modeling workflow (Huang et al., 2022; Nugraha et al., 2022). It is not so obvious to overcome.
137 This observation was the main motivation for putting generic unstructured meshes and complex geometries at the heart
138 of the development of the ComPASS geothermal flow simulator with the ambition to improve the accuracy and the
139 representativeness of numerical models and simulation workflows and facilitate the back and forth between geological
140 modeling and flow modeling.

141 This paper presents the ComPASS code which is an open-source, massively parallel, multi-phase, multi-component
142 flow simulator. The paper focuses on high energy geothermal resources and how generic tetrahedral meshes can be
143 used to exactly match any geological structure including two dimensional elements (geological interfaces, faults or
144 fractures...) or one dimensional sharp features (surface intersections, well trajectories...). Then, adapted numerical
145 schemes can be used in these n -dimensional elements to discretize mass and energy transfers and solve the usual, non-
146 linear balance equations involved in geothermal reservoir modeling. In the following, we may use the term fracture
147 for fracture or fault for brevity regardless of their geological difference.

148 This mixed-dimensional approach is especially useful to take into account fractures that exert a dominant con-
149 trol on subsurface geothermal flows and associated energy transfers. In tectonically active areas, fault zones act as
150 permeable pathways, including high-temperature magmatic environments (Grant and Bixley, 2011; Ingebritsen et al.,
151 2006). But this is also the case in other contexts. Concerning enhanced Geothermal Systems (EGS), where hydraulic

152 stimulation ensures connection with a fault network, flow takes place mostly in a fracture network (Blaisonneau et al.,
153 2021). Role of discontinuities has also been recognized as a significant factor in determining the thermal structure of
154 sedimentary basins, as they can act as conduits linking different aquifer levels (Magri et al., 2010; Person et al., 2012;
155 Simms and Garven, 2004). Geothermal wells are located, so that they intersect faults and fractures (Grant and Bixley,
156 2011). Indeed, the flow dynamics are primarily influenced by the connectivity and conductivity of the fracture network,
157 interacting with the surrounding matrix medium.

158 In terms of software specifications, modeling the non-linear behavior and phase-transitions (boiling and conden-
159 sation) of high-temperature geothermal brines requires quite robust algorithms. The fact that the geological media
160 in which they flow is discontinuous because of the presence of fractures and shows abrupt petrophysical parameters
161 variations over several orders of magnitude, with zonal anisotropies, makes accurate modeling even more challenging.
162 For many years, Tough2 (Pruess et al., 1999; Finsterle et al., 2014) has been a de-facto industry standard (O’Sullivan
163 and O’Sullivan, 2016) mainly thanks to its numerous and versatile *EOS modules* tailored to a large number of physics.
164 Its large community of users contributed to this collection including for example modules for supercritical water con-
165 ditions (Croucher and O’Sullivan, 2008) or brine with dissolved gas (Battistelli et al., 1997).

166 However, many software, including Tough2, use the classical *Two Point Flux Approximation* (TPFA) for spatially
167 discretizing exchange terms in balance equations. TPFA relies on orthogonality conditions and limits the types of
168 acceptable meshes, typically rectangular parallelepipedic boxes in 3D (Eymard et al., 2014). Unfortunately, using
169 coupled finite volume schemes on such structured grids can lead to the Grid Orientation Effect (Eymard et al., 2013).
170 Voronoi diagrams built from unstructured meshes offer more flexibility while maintaining orthogonality (Freeman
171 et al., 2014), but they make the discretization of geological interfaces and intersections challenging, complicating the
172 specification of domain properties and boundary conditions. All code relying on Finite Differences such as SHEMAT
173 (Clauser, 2003) or HYDROTHERM (Hayba and Ingebritsen, 1994) suffer from these constraints as well. By design,
174 Finite Elements based modeling suite handle nicely simplicial meshes, but tools like FEFLOW (Blöcher et al., 2010),
175 COMSOL (Guillou-Frottier et al., 2013; Taillefer et al., 2018) or OpenGeoSys (Kolditz et al., 2012) hardly take into
176 account phase change with boiling or condensation and are consequently not suitable for the modeling of high temper-
177 ature geothermal resources. To handle unstructured meshes, Coumou et al. (2008) implemented an operator splitting
178 approach in the Complex System Modelling Platform (CSMP++) which involves a *thermal equilibrium* step. This
179 approach has then been adapted to model supercritical geothermal resources (Weis et al., 2014).

180 Finally, it is quite common that the discretization of complex 3D geological models with unstructured good quality
181 meshes produces hundreds of thousands to millions of cells, especially when considering regional scale models with
182 many interfaces. In such situation, affordable computation time implies, possibly massive, parallelization of the sim-
183 ulation code. Among the progeny of the Tough2 family of codes, Tough3 (Jung et al., 2017) and the recent Waiwera

184 platform (Croucher et al., 2020) offer such capabilities but suffer from the TPFA scheme limitations. CSMP++ also
 185 comes with High Performance Computing (HPC) capabilities and the DuMu^X platform is based on the modular par-
 186 allel C++ framework Dune (Distributed and Unified Numerics Environment) and handle multi-phase non-isothermal
 187 flows (Koch et al., 2021).

188 The rest of the paper is structured in the following manner. The first part presents the physical model of multi-phase
 189 compositional geothermal flows in fractured geothermal reservoirs and the specific numerical discretizations used in
 190 the ComPASS code. In addition, the approaches used in terms of meshing, parallelization and numerical performances
 191 are summarized. The second part is devoted to numerical tests that demonstrate the benefits of the approach on two
 192 case studies inspired from classical high energy geothermal contexts: a liquid dominated reservoir crossed by major
 193 faults and a steam dominated reservoir.

194 2. Model description

195 In this section, we briefly review the compositional multi-phase model currently implemented in the ComPASS
 196 code as well as related numerical aspects. We refer the interested reader to already published material, especially
 197 Xing et al. (2017); Beaudé et al. (2018); Armandine Les Landes et al. (2023), and to the publicly available code
 198 documentation.

199 2.1. Multi-phase multi-component model

200 2.1.1. Physical system description

201 The description of the physical system is based on a Coats' type formulation Coats (1989) also known as *natural*
 202 *variables formulation*. Considering arbitrary sets of components \mathcal{C} and phases \mathcal{P} , we introduce $\mathcal{C}^\alpha \neq \emptyset$, $\mathcal{C}^\alpha \subset \mathcal{C}$
 203 the set of components that can be present in the phase $\alpha \in \mathcal{P}$ and reciprocally $\mathcal{P}_i \neq \emptyset$, $\mathcal{P}_i \subset \mathcal{P}$ the set of phases
 204 that can contain the component $i \in \mathcal{C}$. Finally, \mathcal{Q} is a finite set of labels, called *contexts*, that are used to describe
 205 different physical states. A simple example of contexts can be $\mathcal{Q} = \{\text{liquid}, \text{gas}, \text{diphasic}\}$. Building on the previous
 206 notations, each context $Q \in \mathcal{Q}$ is then associated to \mathcal{P}_Q , respectively \mathcal{C}_Q , the set of phases, respectively components,
 207 that can be present when considering context Q . It follows that $\overline{\mathcal{C}}_Q = \mathcal{C} \setminus \mathcal{C}_Q$ may be non-empty and designates the
 208 set of components that cannot be present in context Q . This framework is very generic and can be used to describe
 209 very complex fluids.

210 We assume thermal equilibrium between phases so that the thermodynamic characteristics of each phase $\alpha \in \mathcal{P}$ are
 211 influenced by the phase pressure P^α , the temperature T and the phase molar fractions $C^\alpha = (C_i^\alpha)_{i \in \mathcal{C}^\alpha}$. Additionally,
 212 S^α will denote the phase saturation and n_i the number of moles of the component $i \in \mathcal{C}$ per unit pore volume.

Finally, the formulation uses the following set of unknowns:

$$X = ((P^\alpha)_{\alpha \in \mathcal{P}_Q}, T, (C^\alpha)_{\alpha \in \mathcal{P}_Q}, (S^\alpha)_{\alpha \in \mathcal{P}_Q}, (n_i)_{i \in \overline{\mathcal{C}}_Q}, Q). \quad (1)$$

Then, for each context Q the quantity of matter of component $i \in \mathcal{C}_Q$ writes:

$$n_i = \sum_{\alpha \in \mathcal{P}_Q \cap \mathcal{P}_i} \xi^\alpha(P^\alpha, T, C^\alpha) S^\alpha C_i^\alpha$$

with ξ^α the phase molar density, and the fluid internal energy writes:

$$E = \sum_{\alpha \in \mathcal{P}_Q} \xi^\alpha(P^\alpha, T, C^\alpha) S^\alpha e^\alpha(P^\alpha, T, C^\alpha)$$

213 with e^α the phase molar internal energy.

214 2.1.2. Fluxes and conservation laws

Molar and energy conservation provides $\#\mathcal{C} + 1$ balance equations:

$$\begin{cases} \phi \partial_t n_i + \nabla \cdot \mathbf{q}_i = 0, & i \in \mathcal{C}, \\ \phi \partial_t E + (1 - \phi) \partial_t E_r + \nabla \cdot \mathbf{q}_e = 0 \end{cases} \quad (2)$$

where ϕ is the rock porosity assumed constant in time, E_r is the fluid rock energy density. \mathbf{q}_i and \mathbf{q}_e respectively denote the molar flux of component i and the total energy flux comprising advective and diffusive transfers:

$$\begin{aligned} \mathbf{q}_i &= \sum_{\alpha \in \mathcal{P}_Q \cap \mathcal{P}_i} C_i^\alpha \xi^\alpha(P^\alpha, T, C^\alpha) \mathbf{V}^\alpha, \\ \mathbf{q}_e &= \sum_{\alpha \in \mathcal{P}_Q} h^\alpha(P^\alpha, T, C^\alpha) \xi^\alpha(P^\alpha, T, C^\alpha) \mathbf{V}^\alpha - \lambda \nabla T, \\ \mathbf{V}^\alpha &= -\mathbf{K} \frac{k_r^\alpha(S^\alpha)}{\mu^\alpha(P^\alpha, T, C^\alpha)} (\nabla P^\alpha - \rho^\alpha(P^\alpha, T, C^\alpha) \mathbf{g}) \end{aligned}$$

215 which involve the generalized Darcy velocity \mathbf{V}^α , the relative permeability k_r^α , the dynamic viscosity μ^α , the mass
 216 density ρ^α , the molar enthalpy h^α of the phase α , λ the equivalent thermal conductivity of the rock/fluid mixture and
 217 \mathbf{K} the intrinsic rock permeability tensor.

To solve for the unknowns (1), the system (2) is closed by a *flash calculation* that is a fixed point equation which

tracks possible context switches due to phase transitions:

$$Q = Q_{flash}(X). \quad (3)$$

and a set of local closure laws that depend on the current context:

$$\left\{ \begin{array}{l} \sum_{\alpha \in \mathcal{P}_Q} S^\alpha = 1, \\ \sum_{i \in \mathcal{C}^\alpha} C_i^\alpha = 1, \quad \forall \alpha \in \mathcal{P}_Q, \\ P^\alpha - P^\beta = P_c^{\alpha,\beta}(X), \quad \forall (\alpha, \beta) \in \mathcal{P}_Q^2, \alpha \neq \beta, \\ f_i^\alpha(P^\alpha, T, C^\alpha) = f_i^\beta(P^\beta, T, C^\beta), \quad \forall (\alpha, \beta) \in \mathcal{P}_Q^2, \alpha \neq \beta, i \in \mathcal{C}_Q \end{array} \right. \quad (4)$$

218 where $P_c^{\alpha,\beta}(X)$ is a capillary pressure and f_i^α , the fugacity of component i in phase α , is used to write the thermody-
 219 namic equilibrium between phases.

220 2.2. Hybrid model with lower dimension elements

221 In many geothermal applications, the flow is dominated by the connectivity and conductivity of major discon-
 222 tinuities and feedzones are found at their intersections with wells. The main philosophy in ComPASS is to rely on
 223 the versatility of unstructured meshes to exactly match any geological structure and two dimensional geometrical ob-
 224 jects and boundaries (geological interfaces, fractures...) or one dimensional sharp features (surface intersections, well
 225 trajectories...). Depending on the geological model, producing this kind of conformal meshes with relatively good
 226 quality elements can be challenging and it is a crucial step in the whole workflow (Balarac et al., 2022). An alternative,
 227 would be to model lower dimensional entities as with distinct meshes and consider them as *embedded features* which
 228 then adds a complexity in terms of coupling (Cusini et al., 2021).

229 2.2.1. Discrete fractures

230 ComPASS implements a Discrete Fracture Matrix (DFM) method, where fractures are discretized by a subset of
 231 the 3D mesh facets which incorporate a lower-dimensional physical model. The latest is created by averaging the
 232 equations (2), as well as the unknowns (1) related to fractures across their respective widths (Xing et al., 2017).

233 The transmission conditions that exist at the interfaces between the matrix and fractures depend on extra physical
 234 assumptions regarding their drain or barrier behavior of fractures. When they are conductive in terms of both perme-
 235 ability and thermal conductivity, pressure and temperature continuity can be assumed as matrix fracture transmission
 236 conditions in single-phase flows (Serres et al., 2002; Brenner et al., 2016). This approach has been expanded to en-
 237 compass two-phase Darcy flows (Bogdanov et al., 2003; Reichenberger et al., 2006; Brenner et al., 2015, 2017) as well

238 as multi-phase compositional thermal Darcy flows (Xing et al., 2017).

239 **2.2.2. Multi-branch well model**

240 One of the main challenges in well modeling in field simulation is the significant difference between the kilometer
241 scale reservoir and the decimeter scale radius of the wellbore. The well geometry cannot be resolved explicitly by the
242 mesh, so the well is modeled as a line source defined by a one-dimensional graph with a rooted tree structure. This
243 graph can accurately depict sloped and multi-branch wells, and it is discretized by a subset of edges on which the mesh
244 is based.

245 The flow within the well is locally connected to both the 3D matrix surrounding the well and the fractures that
246 intersect the well. The mass and heat exchanges for each node of the well in contact with a fracture or the rock
247 mass are modeled using the Peaceman approach (Peaceman, 1978, 1983). This approach is widely used in reservoir
248 simulation and involves discretizing the Darcy or Fourier fluxes between the reservoir and the well using a two-point
249 flux approximation. The transmissivity takes into account the unresolved pressure or temperature singularity within the
250 well. At the discrete level, the well index or Peaceman's index depends on the type of cell, well radius and geometry,
251 and the discretization scheme used (Wolfsteiner et al., 2003; Aavatsmark and Klausen, 2003; Chen and Zhang, 2009;
252 Yapparova et al., 2022).

253 In the present work, we use an extension of the simple well model detailed by Beaudé et al. (2018) to two-phase
254 flows. The wellbore flow is assumed stationary and by explicitly calculating the pressure drop, the well model is
255 simplified to a single equation with a single implicit unknown which represents the reference pressure of the well.
256 Pressures and saturations along the well are then deduced from this reference pressure and the explicit expression of
257 pressure losses taking into account gravity. To monitor the well, complementary conditions are prescribed between
258 the mass flow rate and the wellhead pressure. For production (resp. injection) wells, they are based on a maximum
259 (resp. minimum) mass flow rate and a minimum (resp. maximum) wellhead pressure. Though a single unknown
260 is introduced, all nodes along the well path are linked to the well reference pressure and this results in additional
261 connectivity in the system, which needs to be taken into account when parallelizing the code (Beaudé et al., 2018).

262 **2.3. Spatial discretization**

263 The discretization of the spatial terms involved in the continuous model introduced previously relies on the Vertex
264 Approximation Gradient (VAG) finite volume scheme (Eymard et al., 2012). This scheme belongs to the family of
265 gradient schemes (Droniou et al., 2010) and is particularly adapted to the resolution of Darcy's law on conformal
266 polyhedral meshes. The VAG discretization has been adapted to mixed-dimensional modeling (Brenner et al., 2016,
267 2015). Two-phase Darcy flows discretization was introduced by Brenner et al. (2015) and generalized to multi-phase
268 multi-component flows by Xing et al. (2017). We approximate Darcy fluxes mobilities using a phase potential upwind

269 scheme.

270 Fig. 1 details the different degrees of freedom introduced by the VAG scheme and their associated fluxes. It shows
 271 one polyhedral cell K (blue) with one fracture face σ (red). The 3D matrix fluxes (blue arrows) connect K to cell
 272 nodes (*e.g.* s, s', s'', s''') and fracture faces when present (*e.g.* σ). The 2D fracture fluxes (red arrows) connect each
 273 fracture face σ to its nodes (*e.g.* s, s'). Finally, nodes that are on a well path (*e.g.* s, s'') are also involved in two-point
 274 fluxes with the well bore flow (green arrow).

275 Then, the volume of each cell is partitioned so that a control volume is associated with each degree of freedom.
 276 Compared to other approaches like Control Volume Finite Element Methods (CVFE), the VAG scheme's crucial ad-
 277 vantage is the flexibility it offers in selecting the control volumes. We exploit it to ensure that there is no mixing of
 278 heterogeneous properties within each control volume nor between matrix and fracture media (Fig. 2) which limits
 279 numerical diffusion.

280 2.4. Numerical aspects

281 2.4.1. Non-linear solver

282 A fully implicit Euler scheme is then used to integrate the semi-discrete problem obtained in Section 2.3 and results
 283 in a non-linear problem with unknowns consisting in reservoir unknowns (1) and a reference pressure for each of the
 284 wells. Because of the flash fixed point equations (eq. (3)) at each degree of freedom, the problem is solved using an
 285 active set Newton-Raphson algorithm (Coats, 1989).

286 As VAG matrix fluxes are expressed linearly and locally to each cell (Fig. 1), the rows of the Jacobian matrix
 287 involved in each Newton iteration and corresponding to the balance equations of the control volumes associated with
 288 cells can be eliminated without any fill-in. Thanks to this elimination, and the use of vertices as main degrees of
 289 freedom during the resolution step, the VAG scheme maintains a comparable cost to nodal methods on unstructured
 290 meshes though it introduces many degrees of freedom (Brenner et al., 2015). It is particularly suitable to work with
 291 tetrahedral meshes that have much more cells than vertices.

292 The size of the Jacobian matrix is also controlled using the discrete version of the local closure equations (4) to
 293 divide the reservoir unknowns into primary and secondary unknowns. The latter are expressed locally as a function of
 294 the former and eliminated from the Jacobian matrix.

295 An iterative solver, typically GMRES, is used to solve the resulting ill-conditioned linear system. A preconditioner
 296 is applied to the solver, which is adapted to the pressure unknown's elliptic or parabolic nature and to the coupling with
 297 the remaining hyperbolic or parabolic unknowns. The CPR-AMG preconditioner is considered to be one of the most
 298 efficient preconditioners for such systems (Lacroix et al., 2001; Scheichl et al., 2003). We refer to Xing et al. (2017)
 299 and Beaudé et al. (2018) for the full details of its implementation.

300 **2.4.2. Parallel implementation**

301 The assembly and resolution of linear systems, which are involved in solving the fully coupled non-linear problem,
 302 are performed in parallel using the Single Program Multiple Data (SPMD) paradigm. The rows of the global system
 303 are distributed in a well balanced manner to available processes (Xing et al., 2017). To be able to assemble these rows,
 304 degrees of freedom holding system unknowns (nodes s , fracture faces σ , cells K and wells w) must also be distributed
 305 between processes, minimizing the need for communications.

306 At the beginning of the simulation, the mesh's cells set is partitioned using the METIS library (Karypis and Kumar,
 307 1998) and each resulting subdomain is linked to a unique process rank. Then, node and fracture degrees of freedom
 308 are distributed to processes according to the cells they are connected to. Elements belonging to the interior of a cell
 309 subdomain are unambiguously attributed to the associated process whereas an arbitrary but reproducible choice is made
 310 for boundary elements (Xing et al., 2017).

311 Ghost elements are added to each subdomain to synchronize unknowns between adjacent degrees of freedom. At
 312 the subdomain boundaries, a single layer of ghost cells is added, along with all the intersecting nodes and fracture
 313 elements (Xing et al., 2017). Concerning wells, reference pressure unknowns are associated to a mesh vertex (node)
 314 and are innately associated with the same process rank as this vertex. However, all nodes that belong to a well path
 315 are created and synchronized across each subdomain that intersects the well path. This approach enables the local re-
 316 computation of well states on any subdomain affected by well operations without requiring communication between
 317 processes (Beaude et al., 2018).

318 Once this distribution is made, meshes are locally reconstructed. At each Newton-Raphson iteration, a linear sys-
 319 tem that corresponds to the rows of the system is created locally on each process using both its own and ghost (*i.e.*
 320 synchronized) unknowns. Once assembled, the system is transferred to the PETSc parallel linear solver library (Balay
 321 et al., 2014). The parallel matrix and vector are stored in PETSc such that each process stores its own rows, which per-
 322 fectly fits our design. The GMRES/CPR-AMG combination outlined previously is implemented using PETSc Krylov
 323 subspace iterative method framework. Following resolution, the ghost unknowns are retrieved through a synchroniza-
 324 tion step using restriction matrices and PETSc matrix-vector product.

325 Scalability tests can be found in Xing et al. (2017) and Armandine Les Landes et al. (2023) and show good behavior
 326 of the ComPASS code with the usual observation that the strong scalability is limited by the AMG-type preconditioner
 327 and requires a sufficiently high number of unknowns per processor (of the order of 10^4 pressure unknowns per proces-
 328 sor).

329 **2.4.3. Application Programming Interface**

330 Whereas previous versions of ComPASS were implemented in pure Fortran, ComPASS 4 introduced a breaking
331 change with the ability to set-up a simulation and control most of the timeloop execution using the high level Python
332 language. The Python layer is not a mere set of routine to pre- or post process data but rather a full Application
333 Programming Interface (API) with the long term ambition to provide a full numerical development environment for
334 reservoir engineers and numerical expert.

335 Building on the simplicity and efficiency of the Python language, one can set-up complex simulations or quickly
336 adapt example scripts or explore simulation results. Some of the physical laws, such as relative permeabilities, capillary
337 pressures, can also be specified by the user directly in Python without the need for compilation, either using an explicit
338 formula or choosing one of the available models. The seasoned user can also build complex physical and/or numerical
339 experiments (Amir and Kern, 2021) without the burden of recompiling the software and without loss of performance.

340 Currently, the simulation outputs are saved as compressed binary NumPy arrays and post-processing routines are
341 provided to convert them to *Paraview* parallel file formats.

342 **2.4.4. Meshing**

343 Though meshing techniques are not the central part of our work, exploiting the full potentialities of the ComPASS
344 code assumes that one is able to generate good-quality conformal meshes out of complex geological models. A con-
345 formal mesh is a mesh such that intersection of any two distinct elements (vertices, edges, faces or cells) is either void
346 either one, and only one, of these elements. Moreover, there are several quality criteria concerning the mesh whose
347 general idea is that the spatial elements are well proportioned not being too flat or distorted. Such ill proportioned
348 elements are well known to create numerical difficulties in reservoir simulation. Though the VAG scheme performs
349 noticeably well on such meshes (Eymard et al., 2011), a good quality mesh will always make the simulation easier,
350 especially when dealing with multi-phase simulations.

351 In the following section, we used *Salome platform* to generate conformal meshes that represent complex geological
352 models. The approach is explicit in the sense that surfaces have been constructed first to represent either faults or
353 layer boundaries. The surfaces composing such a B-Rep (Boundary Representation) model are then meshed with
354 triangles. In a last step the meshing algorithm generates a tetrahedral discretization of the connected components
355 between surface boundaries (Ribes and Caremoli, 2007; Schöberl, 1997). Each of the elements of interest (geological
356 surfaces, fractures, well paths...) are tagged with specific codes using the Salome interface. The codes are then
357 retrieved in the ComPASS simulation using an ad-hoc reader that was developed on purpose and can be used to assign
358 different physical properties. This reader can be easily adapted to any meshing framework.

359 **3. Case studies**

360 ComPASS continuous integration tests include simple synthetic test cases and additional baseline test cases taken
 361 from geothermal code comparison projects (Molloy and Sorey, 1981). These may serve as tutorials and/or template
 362 for new simulations.

363 The next sections focus on two imaginary field studies and highlight the advantages of the ComPASS platform to
 364 describe complex geological settings and various physical conditions of high-energy geothermal resources: a liquid
 365 dominated reservoir crossed by major faults, inspired from the Bouillante geothermal field (Guadeloupe, West Indies)
 366 and a low pressure steam dominated reservoir inspired from the Larderello field (Italy). In both case studies a subcritical
 367 single-component (water) two-phase model is employed with three contexts ($\mathcal{Q} = \{gas, liquid, diphasic\}$).

368 **3.1. Liquid dominated reservoir**

369 **3.1.1. Context, objective and geometry**

370 We consider a 500 m thick liquid-dominated geothermal reservoir, in a volcanic (blue domain in Fig. 3) intersected
 371 by several sub-vertical faults. The reservoir is overlaid by a weakly permeable altered caprock (top yellow domain in
 372 Fig. 3) with a 250 m thickness. The basement layer (bottom yellow domain in Fig. 3), underlies the reservoir.

373 The conformal tetrahedral mesh is made of more than 100,000 nodes and nearly 600,000 cells. Fig. 4 shows 2D
 374 elements (geological horizons and fault surfaces), respectively 1D elements (well paths), discretized by triangle facets,
 375 respectively edges.

376 The geothermal field is operated using a doublet of two deviated wells: a producer (black line in Fig. 4) and an
 377 injector (blue line in Fig. 4). Both wells are open hole in the whole reservoir and intersect the same major fault at
 378 approximately 400 m below surface.

379 **3.1.2. Hydraulic and thermal properties**

380 The caprock and basement layers have low homogeneous and isotropic permeability of 10^{-18} m^2 . The reservoir is
 381 assumed homogeneous and has a 10^{-14} m^2 isotropic permeability and 0.05 porosity. Faults are described by a 10 m
 382 thick damaged area, a $5 \cdot 10^{-14} \text{ m}^2$ permeability and a 0.2 porosity. Upper portions of the faults, that lie in the alteration
 383 zone of the caprock, are treated as having low permeability. The rock thermal properties and density are homogeneous
 384 for the whole rock mass with thermal conductivity $\lambda = 3 \text{ W.K}^{-1} \cdot \text{m}^{-1}$, specific heat capacity $c_p = 1000 \text{ J.kg}^{-1} \cdot \text{K}^{-1}$, and
 385 density $\rho_{rock} = 2600 \text{ kg.m}^{-3}$.

386 **3.1.3. Initial and boundary conditions**

387 Natural state of the geothermal system, is achieved by performing a simulation over a long period of 10^5 years. The
 388 simulation begins with a hydrostatic pressure state of 1 bar at the top of the model, and the temperature field gradually

389 increasing linearly with depth, ranging from 30°C at the top to approximately 280°C at the bottom, until a steady-state
 390 is reached. Temperature and pressure are assigned Dirichlet boundary conditions at the top and bottom boundaries,
 391 while no-flow boundary conditions are imposed on all four lateral boundaries.

392 After 10⁵ years, the geothermal system reaches a stable convective state: the temperature field displays the forma-
 393 tion of convection cells, controlled by the highly permeable faults acting as drains. Iso-temperature surfaces of 190°C
 394 and 250°C highlight this phenomenon (Fig. 5).

395 In this natural state, the geothermal fluid remains liquid throughout the entire domain. The producer well (black
 396 line in Fig. 6) is located close to the intersection of two faults, in order to exploit the warmest (and shallowest) region
 397 located at the apex of an upflowing plume. In this region, the temperature reaches approximately 250°C (Fig. 6.a).

398 **3.1.4. Exploitation scenario**

399 The operating conditions simulation are as follows. The reservoir is first produced with a constant flow rate of
 400 180 ton.hr⁻¹ for a period of three years without reinjection. Then, reinjection begins, with 80% of the produced fluid
 401 being injected back into the reservoir via the injection well, with a wellhead temperature of 110°C. Dirichlet boundary
 402 conditions corresponding to natural state are enforced at the top and bottom boundaries of the domain. Consequently,
 403 the reservoir is not entirely isolated and is partly recharged through the fault network.

404 **3.1.5. Global description of the results**

405 Fig. 6 displays the temporal evolution of the temperature field induced by exploitation near the production area
 406 (left) and the gas saturation (right) at different time steps (0, 2, 3.1, and 20 years).

407 In early stages of production (i.e. prior to the start of injection), the depletion around the producer well favors the
 408 formation of a steam cap in both the reservoir and the fault zones (Fig. 6.b.). As fluid is produced from the reservoir,
 409 the pressure and temperature decrease, resulting in the formation of steam within the reservoir. The steam accumulates
 410 at the top of the reservoir and in the fault zones where the gas saturation is maximum. However, since the caprock part
 411 of the faults is not completely sealed, slight steam migration occurs toward the surface through faults (Fig. 6.b.).

412 The start of injection induces an increase in reservoir pressure and a steam cap contraction while steam around the
 413 injector condenses (Fig. 6.c. vs. Fig. 6.d.). Impact of the reinjection on the steam cap is very quick with the vapor
 414 cloud almost disappearing in 1 month (Fig. 6.d.).

415 After 20 years of production, only a small fraction of steam can be observed in the reservoir near the producer. Note that
 416 the upflowing plume, which is delineated by the isotherm surface of 250°C, has been impacted by the injection
 417 of colder fluid. Its extension is clearly reduced in comparison with the natural state (Fig. 6.d.).

418 The re-injection of fluid at a flow rate of 144 ton.hr⁻¹ (80% of the production) provides an efficient pressure support
 419 and allows to maintain conditions close to the natural state with the vast majority of the reservoir stabilized in liquid

420 state.

421 **3.1.6. Focus on the producer well**

422 Figs. 7, 8, 9 and 10, respectively display the evolution of pressure, specific enthalpy, gas saturation and temperature
423 of the produced fluid in the producer well at a depth equal to that of the reservoir top and in the reservoir at the same
424 depth, over a period of 10 years.

425 In the early stages of production, pressures (in the well and in the reservoir at the top depth) decline rapidly (Fig.
426 7) and result in the production of steam in the well, the gas saturation in the well reaches its maximum value (around
427 0.9) after half a year (Fig. 9). Simultaneously the temperature of the produced fluid decreases from 245 °C to around
428 220°C (Fig. 10), due to the cooling effect of the vaporization. In the meantime, the well specific enthalpy reaches
429 around 1150 kJ/kg, which is higher than the natural state values (Fig. 8) in the reservoir. This excess enthalpy can be
430 explained (Zarrouk and McLean (2019)) by, on one hand, the higher mobility of steam compared to liquid water and on
431 the other hand by an enhanced vaporization of the boiling water in the fractures near the well, ensured by diffusive heat
432 flow from the matrix rock to the fracture fluid. This phenomenon is obviously transient and a decline of the produced
433 fluid enthalpy is then observed (Fig. 8) in conjunction with a slight well gas saturation decrease (Fig. 9).

434 During this period, the hot steam cloud migrates upward to the top of the reservoir where temperature increases
435 (orange curve in Fig. 10) and steam accumulates over time (Fig. 6.b.). This steam cap expansion at the top of the
436 reservoir is characterized by gas saturation reaching its maximum values after two years. Then it decreases due to the
437 decline in boiling (dark red curve in Fig. 9), while the reservoir temperature and pressure are maintained at constant
438 values (Figures 7 and 10).

439 After the injection starts, the producer is quickly impacted due to pressure build-up (Fig. 7) which results in a
440 rapid decrease of gas saturation (around 15%, Fig. 9) and an increase of the temperature of the fluid produced in the
441 well (Fig. 10) and a quick decline of the fluid enthalpy (Fig. 8). From this moment on, operating conditions remain
442 relatively stable.

443 **3.2. Steam-dominated reservoir**

444 **3.2.1. Context, objective and geometry**

445 This section investigates the behavior of a steam dominated reservoir with full reinjection of the produced fluid.
446 The modeled domain measures 2 km x 2 km x 4 km and consists of a reservoir that is 2 km thick, covered by a 2 km
447 thick caprock (respectively blue and yellow domains in Fig. 11). The upper boundary of the reservoir is modeled as
448 a curved surface with a concave shape. The geothermal field is operated with two deviated wells: a steam producer
449 open in the upper section of the reservoir (green in Fig. 11) and an injector which crosses the whole reservoir (blue in
450 Fig. 11).

451 3.2.2. *Hydraulic and thermal properties*

452 The reservoir is assumed to have homogeneous 0.035 porosity and 10^{-14} m² permeability, while the thick overbur-
 453 den has lower values (0.015 porosity and 10^{-20} m² permeability). The rock thermal properties and densities are con-
 454 stant for the whole rock mass with thermal conductivity $\lambda = 2$ W.K⁻¹.m⁻¹, specific heat capacity $c_p = 1000$ J.kg⁻¹.K⁻¹,
 455 and density $\rho_{rock} = 2600$ kg.m⁻³.

456 3.2.3. *Initial and boundary conditions*

457 As a preliminary step, the geothermal system's natural state is obtained by performing a simulation for 10,000
 458 years with the caprock assumed to be initially in a liquid phase, with hydrostatic pressure (atmospheric pressure on
 459 top), and a temperature field increasing linearly with depth (from 30°C at the top to 280°C at the bottom). The reservoir
 460 is assumed to be initially two-phase with constant temperature ($T_{res} = 295^\circ\text{C}$) and gas saturation ($S_g = 0.9$). Dirichlet
 461 boundary conditions are used for temperature and pressure at the top surface (with $T_{top} = 20^\circ\text{C}$ and $P_{top} = 1$ bar), and a
 462 high heat flux of 275 mW.m⁻² is imposed at the bottom boundary (Neumann boundary condition). No flow conditions
 463 are applied on the lateral boundaries.

464 In its natural state, the geothermal system is characterized by a liquid zone at the bottom of the reservoir, while the
 465 remaining part of the reservoir is gas dominated. The caprock is in liquid state (Fig. 12). The pressure in the caprock is
 466 hydrostatic, while the pressure in the reservoir is approximately 80 bars (Fig. 13). The temperature within the caprock
 467 increases linearly with depth and remains constant at around 300°C over the convective part of the reservoir (Figs. 14
 468 and 16).

469 3.2.4. *Exploitation scenario*

470 A constant flow rate of 75 ton.hr⁻¹ is used to produce the reservoir during 30 years. The condensed fluid is fully
 471 reinjected at the wellhead with a temperature of 110°C. Boundary conditions remain the same as for the natural state
 472 computation.

473 Figs. 17, 18 and 19 respectively show the distribution of gas saturation, pressure and temperature at the end of the
 474 exploitation period. A liquid cone has formed at the base of the injection well, which has favored the condensation of
 475 steam around the injector. Figs. 15 and 16 display the vertical profiles of pressure and temperature passing through
 476 the base of the injection well, at both initial and final time.

477 After 30 years of production, the steam pressure has decreased by approximately 23 bars, while the gas-liquid
 478 interface has risen due to the reinjection of cold fluid.

479 4. Conclusions and perspectives

480 We propose a geothermal reservoir 3D modeling workflow based on the use of unstructured conformal meshes to
481 capture the geometries of geological objects (formation interfaces, faults or fractures) or industrial devices (well paths).
482 This choice requires to use an mixed-dimensional model and adapted numerical schemes. Among such schemes, we
483 selected the Vertex Approximate Gradient finite volume scheme which can handle generic polyhedral meshes and has
484 been adapted to mixed-dimensional multi-phase multi-component flows. Moreover, its computational cost depends on
485 the number of vertices of the mesh which makes it particularly interesting for tetrahedral meshes. A parallel version
486 of the VAG scheme was implemented in the ComPASS code with a mixed dimensional multi-phase multi-component
487 physical model relying on a natural variables (*a.k.a.* Coats) formulation. A simple well model, can then be used to
488 simulate geothermal reservoir exploitation scenarios. This capacity has been demonstrated on two case studies inspired
489 for real-world high-energy geothermal fields.

490 In ComPASS version 4, which has been used in this work, a lot of effort has been put in designing a Python API
491 which is not a simple pre- or post-processing layer. Thanks to it, the user is given the possibility of a fine-grained
492 interaction with the numerical workflow, without loss of performance or the need for (re-)compilation. Then, building
493 on the power of the Python ecosystem, complex exploitation workflows can be simulated (cf. simulation scripts used
494 in section 3). The current development efforts focus on different aspects. The well model has been extended to multi-
495 segmented wells with slip velocity between phases, cross-flows, and wall friction and was introduced in ComPASS
496 v4 (Armandine Les Landes et al., 2023). Several physics are developed taking advantage of the generic thermody-
497 namic framework. A diphasic (air-water) module was used to model interactions of an hydrosystem with precipitations
498 (Burnol et al., 2023) whereas specific boundary conditions were developed to take into account exchanges with the
499 atmosphere (Beaude et al., 2019). Additionally, a specific equation of state is currently developed for gas mixtures
500 (Ben Rhouma et al., 2022). Finally, version 5 of ComPASS will consist in a modular refactoring of ComPASS with
501 the overall objective of being able to use simultaneously classical TPFA schemes and more complex scheme such as
502 the VAG scheme (Beaude, 2018).

503 5. Acknowledgments

504 This work was funded by a partnership between BRGM and Storengy (réf. BRGM: RP21DGR054, STORENGY:
505 EISE.DGSM.2021.00117).

506 The postdoctoral work of Daniel Castanon Quiroz was funded by BRGM and Storengy through a joint convention
507 with Université Côte d'Azur (BRGM: 2019/104, STORENGY; STO1927RED, UCA/UNS: 2019/17).

508 The authors wish to acknowledge the use of CaSciModOT high performance computing facilities as part of this
509 research (<https://cascimodot.fr/>).

Code availability

ComPASS is co-developed by BRGM and Université Côte d'Azur (LJAD - Inria) and licensed under GPLv3.

The code is versioned using gitlab. Version 4, which was used in this work, is freely available at:

<https://gitlab.com/compass/compass-v4/compass>.

The corresponding online documentation can be found at: <https://charms.gitlabpages.inria.fr/ComPASS>.

As of today the code runs under Linux OS (possibly through docker or WSL on Windows host system).

To make the installation step smoother we provide a tailored conda environment.

All scripts used to run the simulations presented in section 3 are available on the gitlab platform.

Declaration of Competing Interest

In this paper, the authors state that they have no known financial interests or personal relationships that could have affected the work reported in this study.

References

- Aavatsmark, I., Klausen, R., 2003. Well Index in Reservoir Simulation for Slanted and Slightly Curved Wells in 3D Grids. *SPE Journal* 8, 41–48. URL: <https://doi.org/10.2118/75275-PA>, doi:10.2118/75275-PA, arXiv:<https://onepetro.org/SJ/article-pdf/8/01/41/2124456/spe-75275-pa.pdf>.
- Amir, L., Kern, M., 2021. Jacobian Free Methods for Coupling Transport with Chemistry in Heterogenous Porous Media. *Water* 13. URL: <https://www.mdpi.com/2073-4441/13/3/370>, doi:10.3390/w13030370.
- Armandine Les Landes, A., Castanon Quiroz, D., Jeannin, L., Lopez, S., Masson, R., 2023. Two-phase geothermal model with fracture network and multi-branch wells. *SMAI Journal of Computational Mathematics* URL: <https://hal.science/hal-03273589>.
- Balarac, G., Basile, F., Bénard, P., Bordeu, F., Chapelier, J.B., Cirrottola, L., Caumon, G., Dapogny, C., Frey, P., Froehly, A., Ghigliotti, G., Laraufie, R., Lartigue, G., Legentil, C., Mercier, R., Moureau, V., Nardon, C., Pertant, S., Zakari, M., 2022. Tetrahedral remeshing in the context of large-scale numerical simulation and high performance computing. *MathematicS In Action* 11, 129–164. URL: <https://msia.centre-mersenne.org/articles/10.5802/msia.22/>, doi:10.5802/msia.22.
- Balay, S., Abhyankar, S., Adams, M., Brown, J., Brune, P., Buschelman, K., Eijkhout, V., Gropp, W., Kaushik, D., Knepley, M., et al., 2014. *PETSc Users Manual (Rev. 3.5)*. Technical Report. Argonne National Lab.(ANL), Argonne, IL (United States).
- Battistelli, A., Calore, C., Pruess, K., 1997. The simulator TOUGH2/EWASG for modelling geothermal reservoirs with brines and non-condensable gas. *Geothermics* 26, 437–464. URL: <http://linkinghub.elsevier.com/retrieve/pii/S0375650597000072>, doi:10.1016/S0375-6505(97)00007-2. ISBN: 0375-6505.
- Beaude, L., 2018. Numerical simulation of non-isothermal compositional two-phase flows in porous media and its applications to high energy geothermy. Phd thesis. Université Côte d'Azur. URL: <https://tel.archives-ouvertes.fr/tel-02052110>.
- Beaude, L., Beltzung, T., Brenner, K., Lopez, S., Masson, R., Smai, F., Thebault, J.f., Xing, F., 2018. Parallel Geothermal Numerical Model with Fractures and Multi-Branch Wells. *ESAIM: Proceedings and Surveys* 63, 109–134. URL: <https://hal.archives-ouvertes.fr/hal-01472944https://www.esaim-proc.org/10.1051/proc/201863109>, doi:10.1051/proc/201863109.

- 543 Beaudé, L., Brenner, K., Lopez, S., Masson, R., Smaï, F., 2019. Non-isothermal compositional liquid gas darcy flow: formulation, soil-
544 atmosphere boundary condition and application to high-energy geothermal simulations. *Computational Geosciences* 23, 443–470. doi:10.
545 1007/s10596-018-9794-9.
- 546 Ben Rhouma, S., Smaï, F.F., de Mesquita Lobo Veloso, F., Masson, R., Broseta, D., Chiquet, P., Dossantos, A., 2022. Underground Hydrogen
547 storage with CO₂ cushion gas in aquifers: Which Equation-of-State?, in: *Revitalizing Old Fields and Energy Transition in Mature Basins*,
548 Budapest, Hungary. URL: <https://hal-brgm.archives-ouvertes.fr/hal-03638144>.
- 549 Blaisonneau, A., Maury, J., Armandine Les Landes, A., Guillon, T., 2021. Hydromechanical Modelling of the Hydraulic Stimulation of a Fault
550 Zone as Deep Geothermal Target, in: *World Geothermal Congress*, Reykjavik, Iceland.
- 551 Blöcher, M.G., Zimmermann, G., Moeck, I., Brandt, W., Hassanzadegan, A., Magri, F., 2010. 3D numerical modeling of hydrothermal processes
552 during the lifetime of a deep geothermal reservoir: 3D numerical modeling of hydrothermal processes. *Geofluids* 10, 406–421. URL: <https://onlinelibrary.wiley.com/doi/10.1111/j.1468-8123.2010.00284.x>, doi:10.1111/j.1468-8123.2010.00284.x.
- 553 //onlinelibrary.wiley.com/doi/10.1111/j.1468-8123.2010.00284.x, doi:10.1111/j.1468-8123.2010.00284.x.
- 554 Bogdanov, I.I., Mourzenko, V.V., Thovert, J.F., Adler, P.M., 2003. Two-phase flow through fractured porous media. *Physical Review E* 68.
- 555 Brenner, K., Groza, M., Guichard, C., Lebeau, G., Masson, R., 2016. Gradient discretization of hybrid-dimensional Darcy flows in fractured porous
556 media. *Numerische Mathematik* 134, 569–609.
- 557 Brenner, K., Groza, M., Guichard, C., Masson, R., 2015. Vertex Approximate Gradient scheme for hybrid-dimensional two-phase Darcy flows in
558 fractured porous media. *ESAIM: Mathematical Modelling and Numerical Analysis* 2, 303–330.
- 559 Brenner, K., Groza, M., Jeannin, L., Masson, R., Pellerin, J., 2017. Immiscible two-phase Darcy flow model accounting for vanishing and
560 discontinuous capillary pressures: application to the flow in fractured porous media. *Computational Geosciences* 21, 1075–1094. URL:
561 <https://doi.org/10.1007/s10596-017-9675-7>, doi:10.1007/s10596-017-9675-7.
- 562 Burnol, A., Armandine Les Landes, A., Raucoules, D., Fomelis, M., Allanic, C., Paquet, F., Maury, J., Aochi, H., Guillon, T., Delatre, M.,
563 Dominique, P., Bitri, A., Lopez, S., Pébaÿ, P.P., Bazargan-Sabet, B., 2023. Impacts of Water and Stress Transfers from Ground Surface on the
564 Shallow Earthquake of 11 November 2019 at Le Teil (France). *Remote Sensing* 15, 2270. URL: [https://www.mdpi.com/2072-4292/15/](https://www.mdpi.com/2072-4292/15/9/2270)
565 [9/2270](https://www.mdpi.com/2072-4292/15/9/2270), doi:10.3390/rs15092270.
- 566 Chen, Z., Zhang, Y., 2009. Well Flow Models for Various Numerical Methods. *International Journal of Numerical Analysis and Modeling* 6,
567 375–388. URL: http://global-sci.org/intro/article_detail/ijnam/773.html.
- 568 Clauser, C. (Ed.), 2003. *Numerical Simulation of Reactive Flow in Hot Aquifers*. Springer Berlin Heidelberg, Berlin, Heidelberg. URL: <http://link.springer.com/10.1007/978-3-642-55684-5>, doi:10.1007/978-3-642-55684-5.
- 569 //link.springer.com/10.1007/978-3-642-55684-5, doi:10.1007/978-3-642-55684-5.
- 570 Coats, K.H., 1989. Implicit compositional simulation of single-porosity and dual-porosity reservoirs, in: *SPE symposium on reservoir simulation*,
571 OnePetro. Society of Petroleum Engineers.
- 572 Coumou, D., Matthäi, S., Geiger, S., Driesner, T., 2008. A parallel FE–FV scheme to solve fluid flow in complex geologic media. *Comput-*
573 *ers & Geosciences* 34, 1697–1707. URL: <https://linkinghub.elsevier.com/retrieve/pii/S009830040800112X>, doi:10.1016/j.
574 cageo.2007.11.010.
- 575 Croucher, A., O’Sullivan, M., O’Sullivan, J., Yeh, A., Burnell, J., Kissling, W., 2020. Waiwera: A parallel open-source geothermal flow
576 simulator. *Computers & Geosciences* 141, 104529. URL: <https://linkinghub.elsevier.com/retrieve/pii/S0098300419310088>,
577 doi:10.1016/j.cageo.2020.104529.
- 578 Croucher, A.E., O’Sullivan, M.J., 2008. Application of the computer code TOUGH2 to the simulation of supercritical conditions in geothermal
579 systems. *Geothermics* 37, 622–634. doi:10.1016/j.geothermics.2008.03.005. ISBN: 0375-6505.
- 580 Cusini, M., White, J.A., Castelletto, N., Settigast, R.R., 2021. Simulation of coupled multiphase flow and geomechanics in porous media with

- 581 embedded discrete fractures. *International Journal for Numerical and Analytical Methods in Geomechanics* 45, 563–584. URL: [https://](https://onlineibrary.wiley.com/doi/10.1002/nag.3168)
 582 onlineibrary.wiley.com/doi/10.1002/nag.3168, doi:10.1002/nag.3168.
- 583 Daniilidis, A., Saeid, S., Doonechaly, N.G., 2021. The fault plane as the main fluid pathway: Geothermal field development options under sub-
 584 surface and operational uncertainty. *Renewable Energy* 171, 927–946. URL: [https://www.sciencedirect.com/science/article/pii/](https://www.sciencedirect.com/science/article/pii/S096014812100327X)
 585 [S096014812100327X](https://www.sciencedirect.com/science/article/pii/S096014812100327X), doi:<https://doi.org/10.1016/j.renene.2021.02.148>.
- 586 Droniou, J., Eymard, R., Gallouët, T., Herbin, R., 2010. A unified approach to mimetic finite difference, hybrid finite volume and mixed finite
 587 volume methods. *Math. Models Methods Appl. Sci.* 20, 265–295. URL: <http://dx.doi.org/10.1142/S0218202510004222>, doi:10.
 588 [1142/S0218202510004222](http://dx.doi.org/10.1142/S0218202510004222).
- 589 Eymard, R., Gallouët, T., Guichard, C., Herbin, R., Masson, R., 2014. TP or not TP, that is the question. *Computational Geosciences* 18, 285–296.
 590 URL: <http://link.springer.com/10.1007/s10596-013-9392-9>, doi:10.1007/s10596-013-9392-9.
- 591 Eymard, R., Guichard, C., Herbin, R., 2011. Benchmark 3D: the VAG scheme, in: Fořt, J., Fürst, J., Halama, J., Herbin, R., Hubert, F. (Eds.), *Finite*
 592 *Volumes for Complex Applications VI Problems & Perspectives*, Springer Berlin Heidelberg, Berlin, Heidelberg. pp. 1013–1022.
- 593 Eymard, R., Guichard, C., Herbin, R., 2012. Small-stencil 3D schemes for diffusive flows in porous media. *ESAIM: Mathematical Modelling and*
 594 *Numerical Analysis* 46, 265–290.
- 595 Eymard, R., Guichard, C., Masson, R., 2013. Grid orientation effect in coupled finite volume schemes. *IMA Journal of Numerical Analysis* 33, 582–
 596 608. URL: <https://academic.oup.com/imajna/article-lookup/doi/10.1093/imanum/drs016>, doi:10.1093/imanum/drs016.
- 597 Finsterle, S., Sonnenthal, E.L., Spycher, N., 2014. Advances in subsurface modeling using the TOUGH suite of simulators. *Computers & Geo-*
 598 *sciences* 65, 2–12. URL: <http://linkinghub.elsevier.com/retrieve/pii/S0098300413001738>, doi:10.1016/j.cageo.2013.06.
 599 009. publisher: Elsevier.
- 600 Freeman, C., Boyle, K., Reagan, M., Johnson, J., Rycroft, C., Moridis, G., 2014. MeshVoro: A three-dimensional Voronoi mesh building tool
 601 for the TOUGH family of codes. *Computers & Geosciences* 70, 26–34. URL: [https://linkinghub.elsevier.com/retrieve/pii/](https://linkinghub.elsevier.com/retrieve/pii/S0098300414001046)
 602 [S0098300414001046](https://linkinghub.elsevier.com/retrieve/pii/S0098300414001046), doi:10.1016/j.cageo.2014.05.002.
- 603 Grant, M.A., Bixley, P.F., 2011. Preface to the second edition, in: Grant, M.A., Bixley, P.F. (Eds.), *Geothermal Reservoir Engineering (Second*
 604 *Edition)*. second edition ed.. Academic Press, Boston, pp. xv–xvi. URL: [https://www.sciencedirect.com/science/article/pii/](https://www.sciencedirect.com/science/article/pii/B9780123838803100253)
 605 [B9780123838803100253](https://www.sciencedirect.com/science/article/pii/B9780123838803100253), doi:<https://doi.org/10.1016/B978-0-12-383880-3.10025-3>.
- 606 Guillou-Frottier, L., Carré, C., Bourguin, B., Bouchot, V., Genter, A., 2013. Structure of hydrothermal convection in the Upper Rhine Graben as
 607 inferred from corrected temperature data and basin-scale numerical models. *Journal of Volcanology and Geothermal Research* 256, 29–49. URL:
 608 <https://linkinghub.elsevier.com/retrieve/pii/S0377027313000590>, doi:10.1016/j.jvolgeores.2013.02.008.
- 609 Hayba, D., Ingebritsen, S.E., 1994. The computer model Hydrotherm, a three-dimensional finite-difference model to simulate ground-water flow and
 610 heat transport in the temperature range of 0 to 1,200 degrees C. Technical Report 94-4045. URL: [http://pubs.er.usgs.gov/publication/](http://pubs.er.usgs.gov/publication/wri944045)
 611 [wri944045](http://pubs.er.usgs.gov/publication/wri944045), doi:10.3133/wri944045.
- 612 Hirschberg, S., Wiemer, S., Burgherr, P., 2014. Energy from the Earth: Deep Geothermal as a Resource for the Future?. volume 62. vdf Hochschul-
 613 verlag AG.
- 614 Huang, Y., Cheng, Y., Ren, L., Tian, F., Pan, S., Wang, K., Wang, J., Dong, Y., Kong, Y., 2022. Assessing the geothermal resource potential
 615 of an active oil field by integrating a 3d geological model with the hydro-thermal coupled simulation. *Frontiers in Earth Science* 9. URL:
 616 <https://www.frontiersin.org/article/10.3389/feart.2021.787057>, doi:10.3389/feart.2021.787057.
- 617 Ingebritsen, S.E., Geiger, S., Hurwitz, S., Driesner, T., 2010. Numerical simulation of magmatic hydrothermal systems. *Reviews of Geophysics*
 618 48, RG1002. URL: <http://dx.doi.org/10.1029/2009RG000287>, doi:10.1029/2009RG000287. publisher: AGU.

- 619 Ingebritsen, S.E., Sanford, W.E., Neuzil, C.E., 2006. Groundwater in geologic processes, 2nd edition. Cambridge University Press.
- 620 International Renewable Energy Agency, International Geothermal Association, 2023. Global geothermal mar-
621 ket and technology assessment. Technical Report. URL: [https://www.irena.org/Publications/2023/Feb/](https://www.irena.org/Publications/2023/Feb/Global-geothermal-market-and-technology-assessment)
622 [Global-geothermal-market-and-technology-assessment](https://www.irena.org/Publications/2023/Feb/Global-geothermal-market-and-technology-assessment).
- 623 Jalilinasrabad, S., Tanaka, T., Itoi, R., Goto, H., 2021. Numerical simulation and production prediction assessment of takigami geothermal
624 reservoir. Energy 236, 121503. URL: <https://www.sciencedirect.com/science/article/pii/S0360544221017515>, doi:<https://doi.org/10.1016/j.energy.2021.121503>.
- 625 [//doi.org/10.1016/j.energy.2021.121503](https://doi.org/10.1016/j.energy.2021.121503).
- 626 Jung, Y., Pau, G.S.H., Finsterle, S., Pollyea, R.M., 2017. TOUGH3: A new efficient version of the TOUGH suite of multiphase flow and trans-
627 port simulators. Computers & Geosciences 108, 2–7. URL: <https://linkinghub.elsevier.com/retrieve/pii/S00983300416304319>,
628 doi:[10.1016/j.cageo.2016.09.009](https://doi.org/10.1016/j.cageo.2016.09.009).
- 629 Karypis, G., Kumar, V., 1998. A Fast and high quality multilevel scheme for partitioning irregular graphs. SIAM Journal on Scientific Computing
630 20, 359–392.
- 631 Koch, T., Gläser, D., Weishaupt, K., Ackermann, S., Beck, M., Becker, B., Burbulla, S., Class, H., Coltman, E., Emmert, S., Fetzner, T., Grüninger, C.,
632 Heck, K., Hommel, J., Kurz, T., Lipp, M., Mohammadi, F., Scherrer, S., Schneider, M., Seitz, G., Stadler, L., Utz, M., Weinhardt, F., Flemisch, B.,
633 2021. DuMux 3 – an open-source simulator for solving flow and transport problems in porous media with a focus on model coupling. Computers &
634 Mathematics with Applications 81, 423–443. URL: <https://linkinghub.elsevier.com/retrieve/pii/S0898122120300791>, doi:[10.1016/j.camwa.2020.02.012](https://doi.org/10.1016/j.camwa.2020.02.012).
- 635 [1016/j.camwa.2020.02.012](https://doi.org/10.1016/j.camwa.2020.02.012).
- 636 Kolditz, O., Bauer, S., Bilke, L., Böttcher, N., Delfs, J.O., Fischer, T., Görke, U.J., Kalbacher, T., Kosakowski, G., McDermott, C.I., Park, C.H., Radu,
637 F., Rink, K., Shao, H., Shao, H.B., Sun, F., Sun, Y.Y., Singh, A.K., Taron, J., Walther, M., Wang, W., Watanabe, N., Wu, Y., Xie, M., Xu, W.,
638 Zehner, B., 2012. OpenGeoSys: an open-source initiative for numerical simulation of thermo-hydro-mechanical/chemical (THM/C) processes in
639 porous media. Environmental Earth Sciences 67, 589–599. URL: <http://link.springer.com/10.1007/s12665-012-1546-x>, doi:[10.1007/s12665-012-1546-x](https://doi.org/10.1007/s12665-012-1546-x).
- 640 [1007/s12665-012-1546-x](https://doi.org/10.1007/s12665-012-1546-x).
- 641 Lacroix, S., Vassilevski, Y.V., Wheeler, M.F., 2001. Decoupling preconditioners in the implicit parallel accurate reservoir simulator (IPARS).
642 Numerical Linear Algebra with Applications 8, 537–549.
- 643 Lopez, S., Calcagno, P., Þorsteinsdóttir, U., Páll Hersir, G., Manzella, A., 2017. Thoughts on integrated modeling of magmatic geothermal
644 fields, in: IMAGE Final Conference, Akureyri, Iceland. p. 45. URL: [http://www.image-fp7.fr/reference-documents/deliverables/](http://www.image-fp7.fr/reference-documents/deliverables/IMAGE-D2.08-2017.10.04-06-Final-Conference-Abstracts-public.pdf)
645 [IMAGE-D2.08-2017.10.04-06-Final-Conference-Abstracts-public.pdf](http://www.image-fp7.fr/reference-documents/deliverables/IMAGE-D2.08-2017.10.04-06-Final-Conference-Abstracts-public.pdf).
- 646 Magri, F., Akar, T., Gemici, U., Pekdeger, A., 2010. Deep geothermal groundwater flow in the seferihisar-bağcova area,
647 turkey: results from transient numerical simulations of coupled fluid flow and heat transport processes. Geofluids 10, 388–405.
648 URL: <https://onlinelibrary.wiley.com/doi/abs/10.1111/j.1468-8123.2009.00267.x>, doi:[https://doi.org/10.1111/j.](https://doi.org/10.1111/j.1468-8123.2009.00267.x)
649 [1468-8123.2009.00267.x](https://doi.org/10.1111/j.1468-8123.2009.00267.x), arXiv:<https://onlinelibrary.wiley.com/doi/pdf/10.1111/j.1468-8123.2009.00267.x>.
- 650 Molloy, M.W., Sorey, M.L., 1981. Code Comparison Project – A Contribution to Confidence in Geothermal Reservoir Simulators. Geothermal
651 Resources Council Transactions .
- 652 Nugraha, R., O’Sullivan, J., O’Sullivan, M., Abdurachman, F., 2022. Geothermal Modelling: Industry Standard Practices, in: 47th Workshop
653 on Geothermal Reservoir Engineering, Stanford, California. URL: [https://pangea.stanford.edu/ERE/pdf/IGastandard/SGW/2022/](https://pangea.stanford.edu/ERE/pdf/IGastandard/SGW/2022/Nugraha.pdf)
654 [Nugraha.pdf](https://pangea.stanford.edu/ERE/pdf/IGastandard/SGW/2022/Nugraha.pdf).
- 655 O’Sullivan, M., O’Sullivan, J., 2016. Reservoir modeling and simulation for geothermal resource characterization and evaluation, in: Geothermal
656 Power Generation. Elsevier, pp. 165–199. URL: <https://linkinghub.elsevier.com/retrieve/pii/B9780081003374000073>, doi:[10.1016/B9780081003374000073](https://doi.org/10.1016/B9780081003374000073).

- 1016/B978-0-08-100337-4.00007-3.
- O'Sullivan, M.J., Pruess, K., Lippmann, M.J., 2001. State of the art of geothermal reservoir simulation. *Geothermics* 30, 395–429. URL: <https://linkinghub.elsevier.com/retrieve/pii/S0375650501000050>, doi:10.1016/S0375-6505(01)00005-0.
- O'Sullivan, M.J., Yeh, A., Mannington, W.I., 2009. A history of numerical modelling of the Wairakei geothermal field. *Geothermics* 38, 155–168. URL: <https://linkinghub.elsevier.com/retrieve/pii/S0375650508000849>, doi:10.1016/j.geothermics.2008.12.001.
- Peaceman, D., 1978. Interpretation of Well-Block Pressures in Numerical Reservoir Simulation. *Society of Petroleum Engineers Journal* 18, 183–194. URL: <https://onepetro.org/spejournal/article/18/03/183/168105/Interpretation-of-Well-Block-Pressures-in>, doi:10.2118/6893-PA.
- Peaceman, D.W., 1983. Interpretation of Well-Block Pressures in Numerical Reservoir Simulation With Nonsquare Grid Blocks and Anisotropic Permeability. *Society of Petroleum Engineers Journal* 23, 531–543. URL: <https://onepetro.org/spejournal/article/23/03/531/69233/Interpretation-of-Well-Block-Pressures-in>, doi:10.2118/10528-PA.
- Person, M., Hofstra, A., Sweetkind, D., Stone, W., Cohen, D., Gable, C.W., Banerjee, A., 2012. Analytical and numerical models of hydrothermal fluid flow at fault intersections. *Geofluids* 12, 312–326. URL: <https://onlinelibrary.wiley.com/doi/abs/10.1111/gfl.12002>, doi:<https://doi.org/10.1111/gfl.12002>, arXiv:<https://onlinelibrary.wiley.com/doi/pdf/10.1111/gfl.12002>.
- Pruess, K., Oldenburg, C., Moridis, G., 1999. TOUGH2 user's guide, version 2. Technical Report. Earth Sciences Division, Lawrence Berkeley National Laboratory, University of California. URL: http://esd.lbl.gov/files/research/projects/tough/documentation/TOUGH2_V2_Users_Guide.pdf. backup Publisher: Earth Sciences Division, Lawrence Berkeley National Laboratory, University of California Issue: LBNL-43134 Volume: LBNL-43134.
- Reichenberger, V., Jakobs, H., Bastian, P., Helmig, R., 2006. A mixed-dimensional finite volume method for two-phase flow in fractured porous media. *Advances in Water Resources* 29, 1020–1036.
- Ribes, A., Caremoli, C., 2007. Salomé platform component model for numerical simulation, in: 31st Annual International Computer Software and Applications Conference (COMPSAC 2007), pp. 553–564. doi:10.1109/COMPSAC.2007.185.
- Scheichl, R., Masson, R., Wendebourg, J., 2003. Decoupling and block preconditioning for sedimentary basin simulations. *Computational Geosciences* 7, 295–318.
- Schöberl, J., 1997. Netgen an advancing front 2d/3d-mesh generator based on abstract rules. *Computing and Visualization in Science* 1, 41–52. URL: <https://www.sciencedirect.com/science/article/pii/S096014812100327X>, doi:<https://doi.org/10.1007/s007910050004>.
- Serres, C., Alboin, C., Jaffre, J., Roberts, J., 2002. Modeling fractures as interfaces for flow and transport in porous media. Technical Report. Inst. de Radioprotection et de Surete Nucleaire.
- Simms, M.A., Garven, G., 2004. Thermal convection in faulted extensional sedimentary basins: theoretical results from finite-element modeling. *Geofluids* 4, 109–130. URL: <https://onlinelibrary.wiley.com/doi/abs/10.1111/j.1468-8115.2004.00069.x>, doi:<https://doi.org/10.1111/j.1468-8115.2004.00069.x>, arXiv:<https://onlinelibrary.wiley.com/doi/pdf/10.1111/j.1468-8115.2004.00069.x>.
- Taillefer, A., Guillou-Frottier, L., Soliva, R., Magri, F., Lopez, S., Courrioux, G., Millot, R., Ladouche, B., Le Goff, E., 2018. Topographic and Faults Control of Hydrothermal Circulation Along Dormant Faults in an Orogen. *Geochemistry, Geophysics, Geosystems* URL: <https://onlinelibrary.wiley.com/doi/abs/10.1029/2018GC007965>, doi:10.1029/2018GC007965.
- Weis, P., Driesner, T., Coumou, D., Geiger, S., 2014. Hydrothermal, multiphase convection of H₂O-NaCl fluids from ambient to magmatic temperatures: a new numerical scheme and benchmarks for code comparison. *Geofluids* 14, 347–371. URL: <https://onlinelibrary>.

- 695 wiley.com/doi/10.1111/gf1.12080, doi:10.1111/gf1.12080.
- 696 Wolfsteiner, C., Durlofsky, L.J., Aziz, K., 2003. Calculation of well index for nonconventional wells on arbitrary grids. *Computational Geosciences*
697 7, 61–82. URL: <https://doi.org/10.1023/A:1022431729275>, doi:10.1023/A:1022431729275.
- 698 Xing, F., Masson, R., Lopez, S., 2017. Parallel numerical modeling of hybrid-dimensional compositional non-isothermal darcy flows in fractured
699 porous media. *Journal of Computational Physics* 345, 637–664. doi:10.1016/j.jcp.2017.05.043.
- 700 Yapparova, A., Lamy-Chappuis, B., Scott, S.W., Driesner, T., 2022. A Peaceman-type well model for the 3D Control Volume Finite Element
701 Method and numerical simulations of supercritical geothermal resource utilization. *Geothermics* 105, 102516. URL: <https://linkinghub.elsevier.com/retrieve/pii/S0375650522001614>, doi:10.1016/j.geothermics.2022.102516.
- 702
- 703 Zarrouk, S.J., McLean, K., 2019. Chapter 2 - geothermal systems, in: Zarrouk, S.J., McLean, K. (Eds.), *Geothermal Well Test Analysis*. Academic
704 Press, pp. 13–38. URL: <https://www.sciencedirect.com/science/article/pii/B9780128149461000025>, doi:<https://doi.org/10.1016/B978-0-12-814946-1.00002-5>.
- 705

706 **List of Figures**

707 1 For a cell K and a fracture face σ (in bold), examples of VAG degrees of freedom $u_K, u_S, u_{S'}, u_\sigma$ and
708 VAG fluxes $F_{K,\sigma}, F_{K,S}, F_{K,S'}, F_{\sigma,S}$ 23
709 2 Example of control volumes at cells, fracture face, and nodes, in the case of two cells K and L split
710 by one fracture face σ (the width of the fracture is enlarged in this figure). The control volumes are
711 chosen to avoid mixing fracture and matrix rocktypes. 24
712 3 Geometry and mesh of the domain modeled 25
713 4 Mesh and wells location 26
714 5 Isotemperature surfaces of 50°C, 190°C and 250°C at the initial state, dominated by convection. . . . 27
715 6 Left: Temperature evolution (°C) at multiple times within the faults and within the domain (isotem-
716 perature surface of 250°C). Right: Gas saturation evolution (isosaturation surface of 0.1) at multiple
717 times: 0, 2, 3.1 and 20 years. 28
718 7 Pressure at the top depth in the producer well and in the reservoir as function of time 29
719 8 Energy flow rate at the top depth in the producer well and in the reservoir as function of time 30
720 9 Gas saturation at the top depth in the producer well and in the reservoir as function of time 31
721 10 Temperature at the top depth in the producer well and in the reservoir as function of time 32
722 11 Domain modeled with the reservoir (in blue) and the caprock (in yellow), the mesh and the wells
723 location : injector (in blue) and producer (in green). 33
724 12 Gas saturation at the initial state of the steam-dominated reservoir. 34
725 13 Pressure distribution at the initial state of the steam-dominated reservoir. 35
726 14 Temperature (°C) distribution at the initial state of the steam-dominated reservoir. 36
727 15 Vertical pressure profiles (passing through the base of the injection well) - blue: initial pressure - red:
728 after 30 years of production 37
729 16 Vertical temperature profiles (passing through the base of the injection well) - blue: initial temperature
730 - red: after 30 years of production. 38
731 17 Gas saturation within the reservoir after 30 years of production. 39
732 18 Pressure distribution within the reservoir after 30 years of production. 40
733 19 Temperature distribution (°C) within the reservoir after 30 years of production. 41

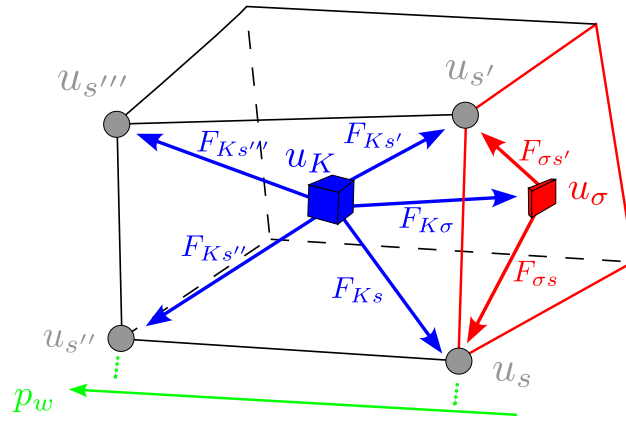


Figure 1: For a cell K and a fracture face σ (in bold), examples of VAG degrees of freedom $u_K, u_S, u_{S'}, u_\sigma$ and VAG fluxes $F_{K,\sigma}, F_{K,S}, F_{K,S'}, F_{\sigma,S}$.

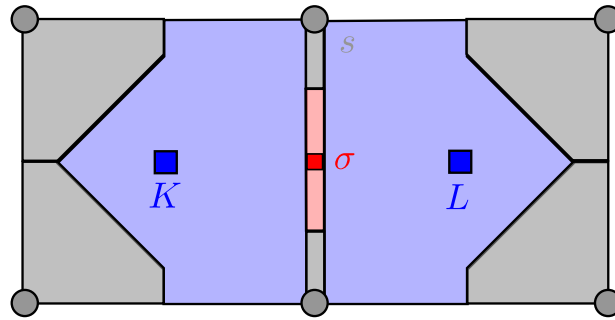


Figure 2: Example of control volumes at cells, fracture face, and nodes, in the case of two cells K and L split by one fracture face σ (the width of the fracture is enlarged in this figure). The control volumes are chosen to avoid mixing fracture and matrix rocktypes.

Geothermal Modeling with ComPASS

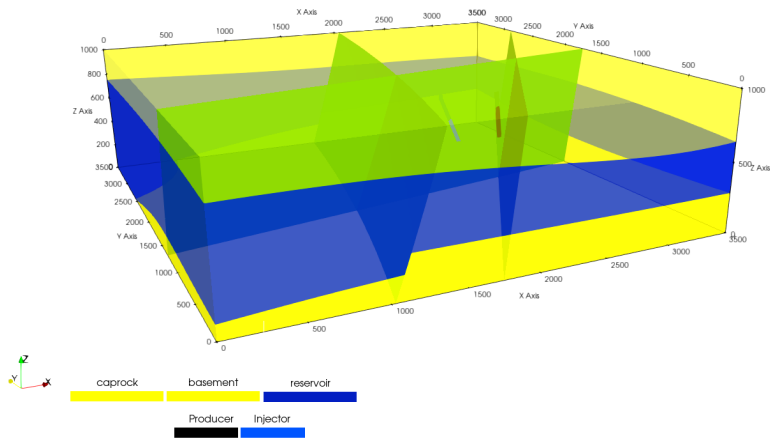


Figure 3: Geometry and mesh of the domain modeled

Geothermal Modeling with ComPASS

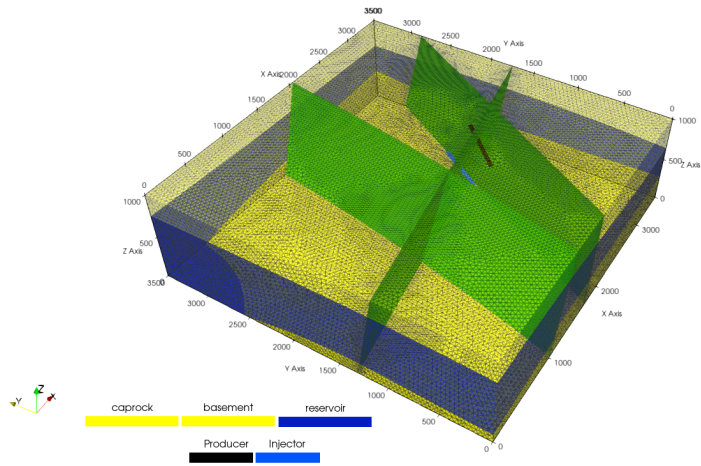


Figure 4: Mesh and wells location

Geothermal Modeling with ComPASS

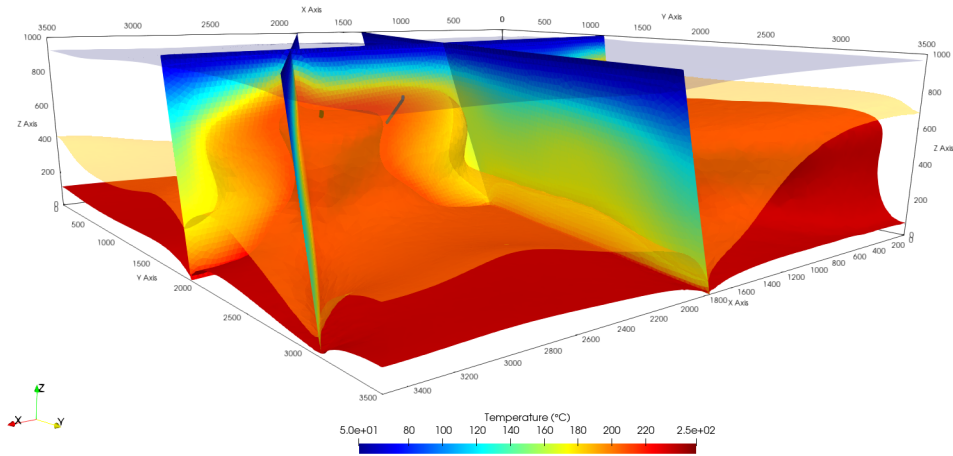


Figure 5: Isotherm surfaces of 50°C, 190°C and 250°C at the initial state, dominated by convection.

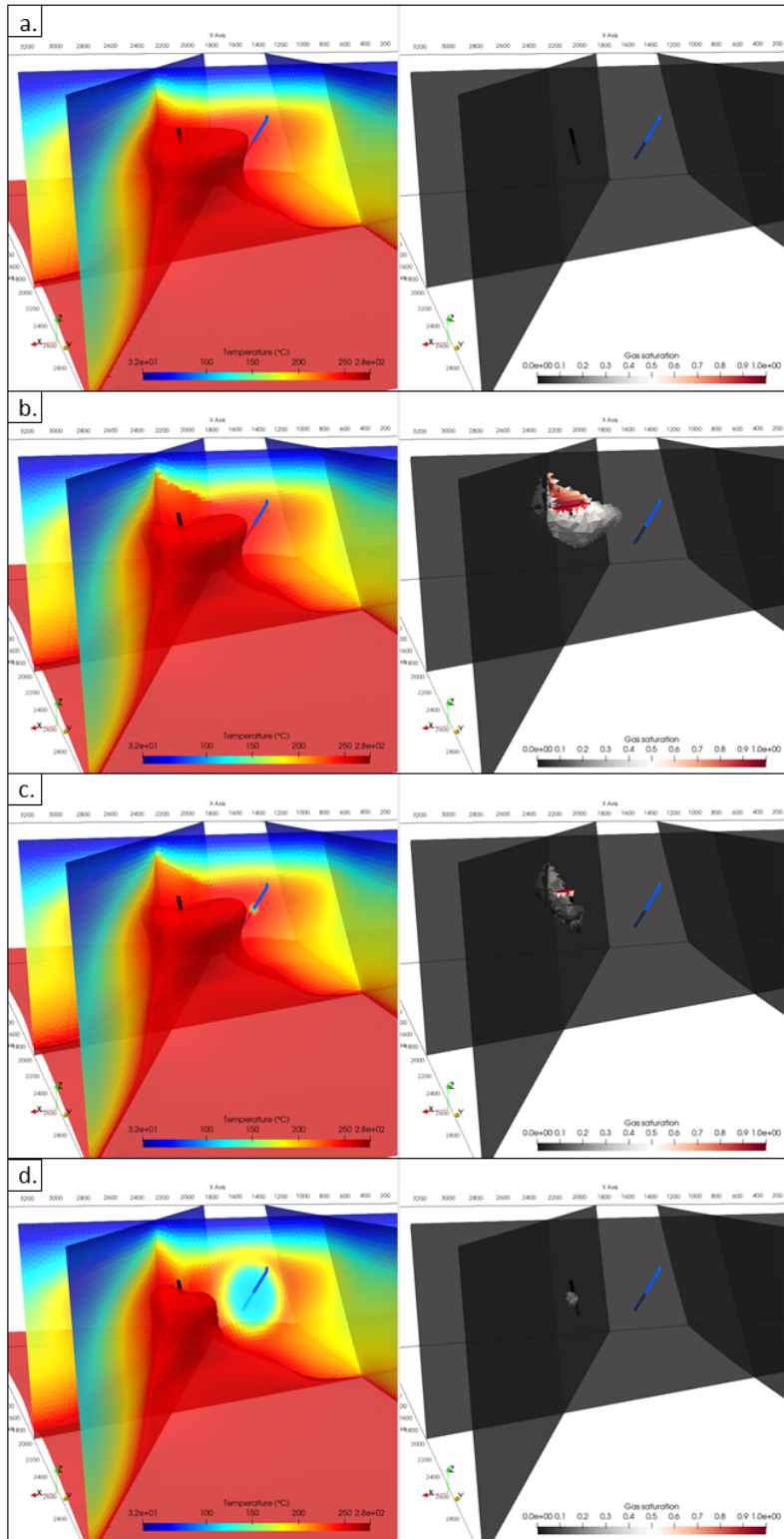


Figure 6: Left: Temperature evolution ($^{\circ}\text{C}$) at multiple times within the faults and within the domain (isotemperature surface of 250°C). Right: Gas saturation evolution (isosaturation surface of 0.1) at multiple times: 0, 2, 3.1 and 20 years.

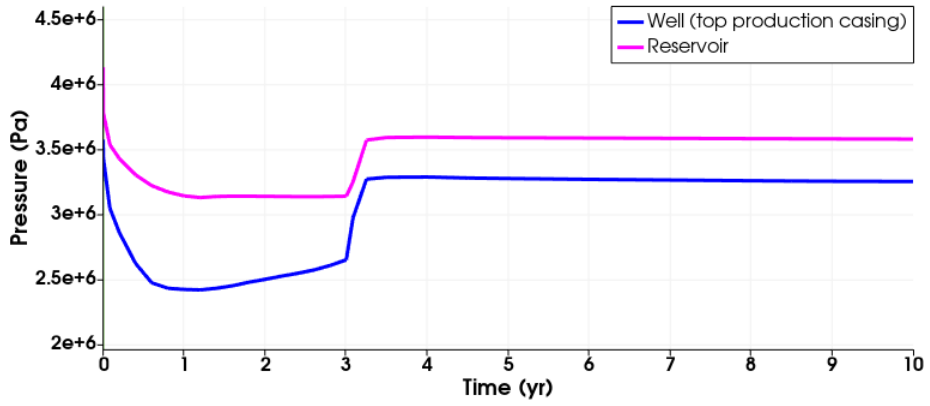


Figure 7: Pressure at the top depth in the producer well and in the reservoir as function of time

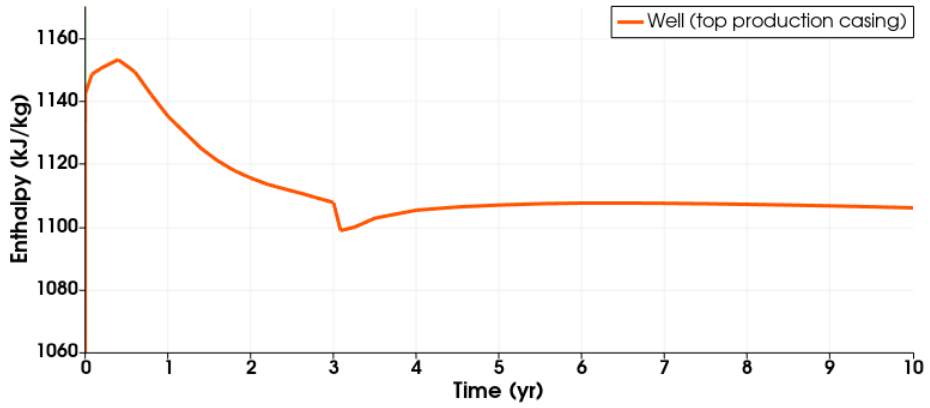


Figure 8: Energy flow rate at the top depth in the producer well and in the reservoir as function of time

Geothermal Modeling with ComPASS

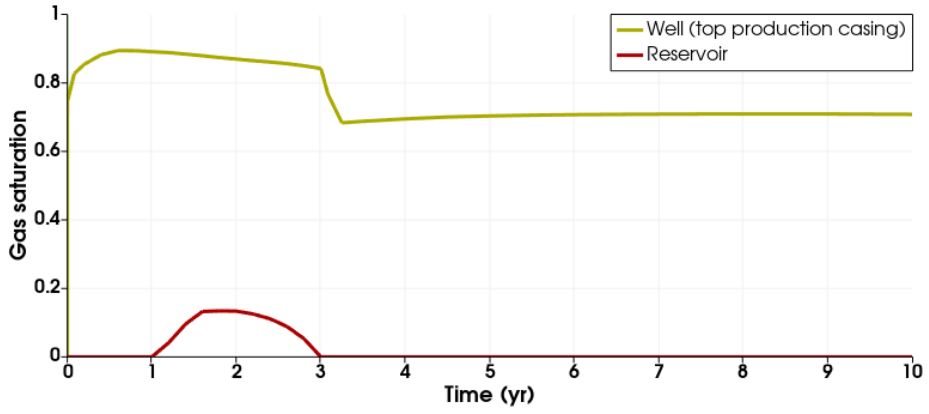


Figure 9: Gas saturation at the top depth in the producer well and in the reservoir as function of time

Geothermal Modeling with ComPASS

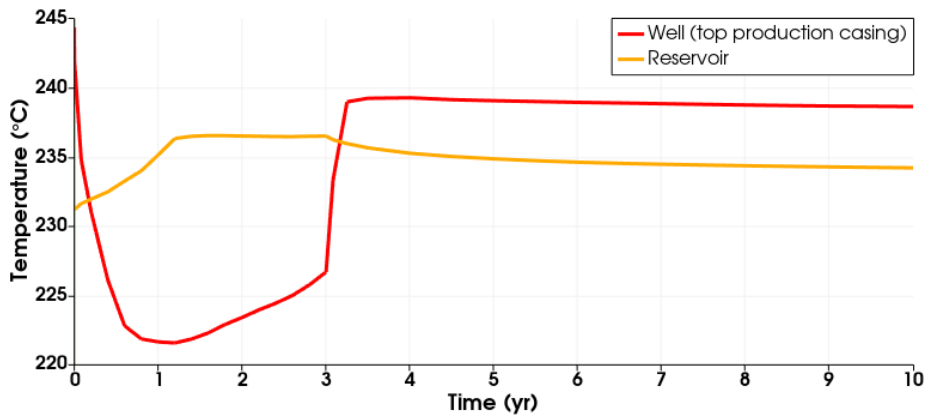


Figure 10: Temperature at the top depth in the producer well and in the reservoir as function of time

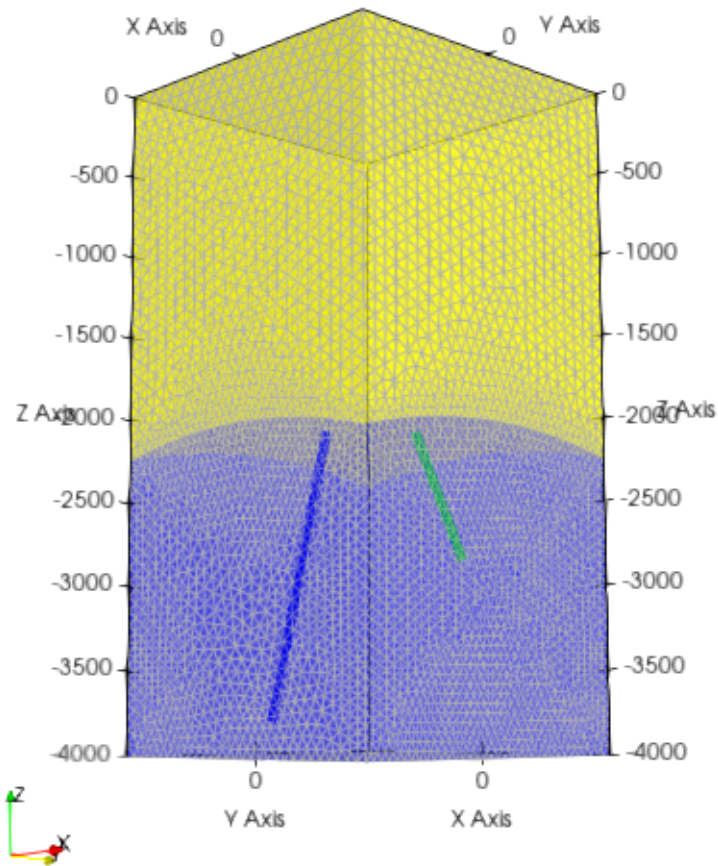


Figure 11: Domain modeled with the reservoir (in blue) and the caprock (in yellow), the mesh and the wells location : injector (in blue) and producer (in green).

Geothermal Modeling with ComPASS

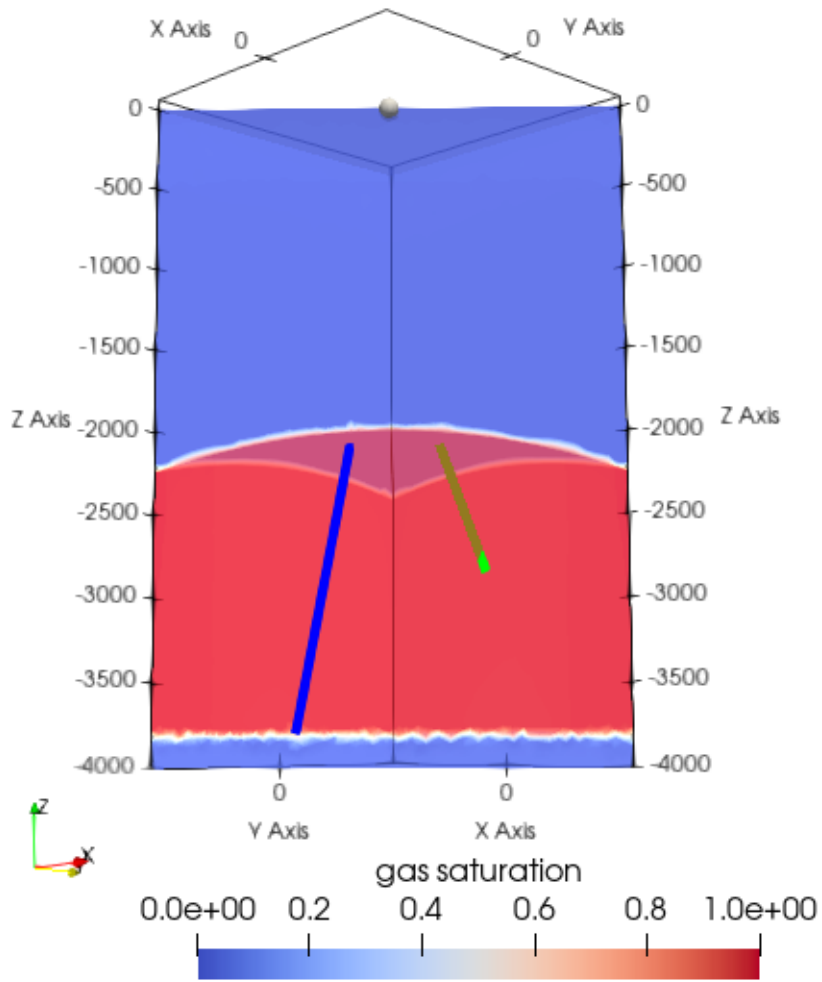


Figure 12: Gas saturation at the initial state of the steam-dominated reservoir.

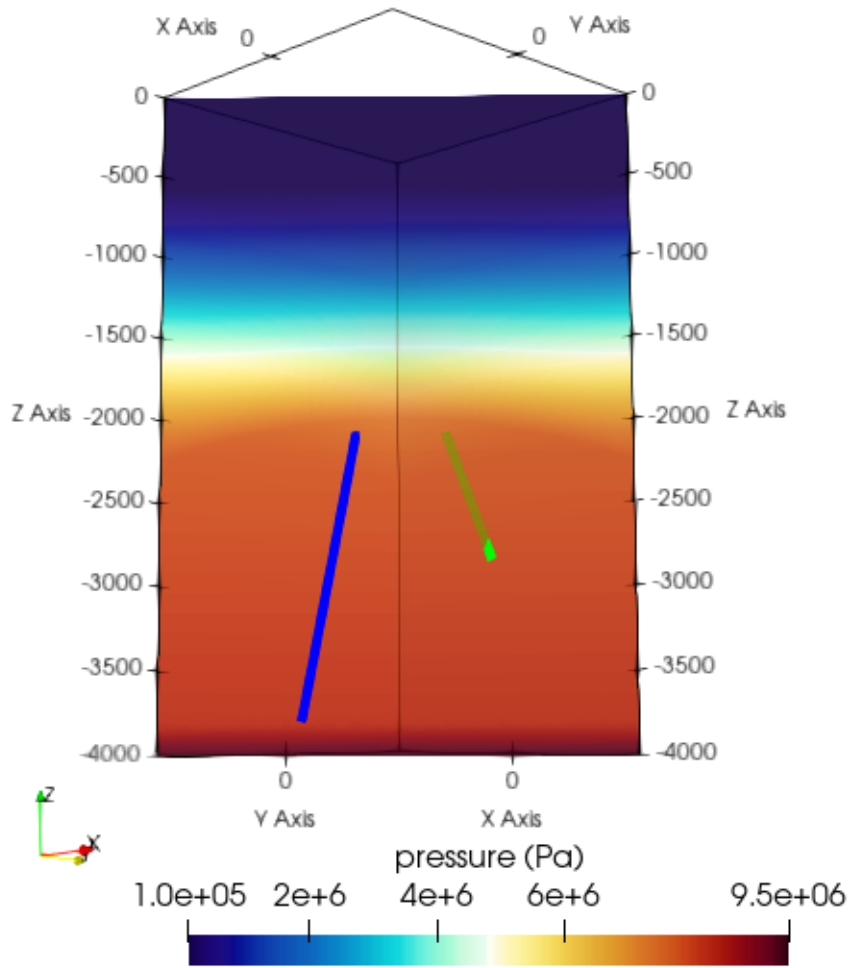


Figure 13: Pressure distribution at the initial state of the steam-dominated reservoir.

Geothermal Modeling with ComPASS

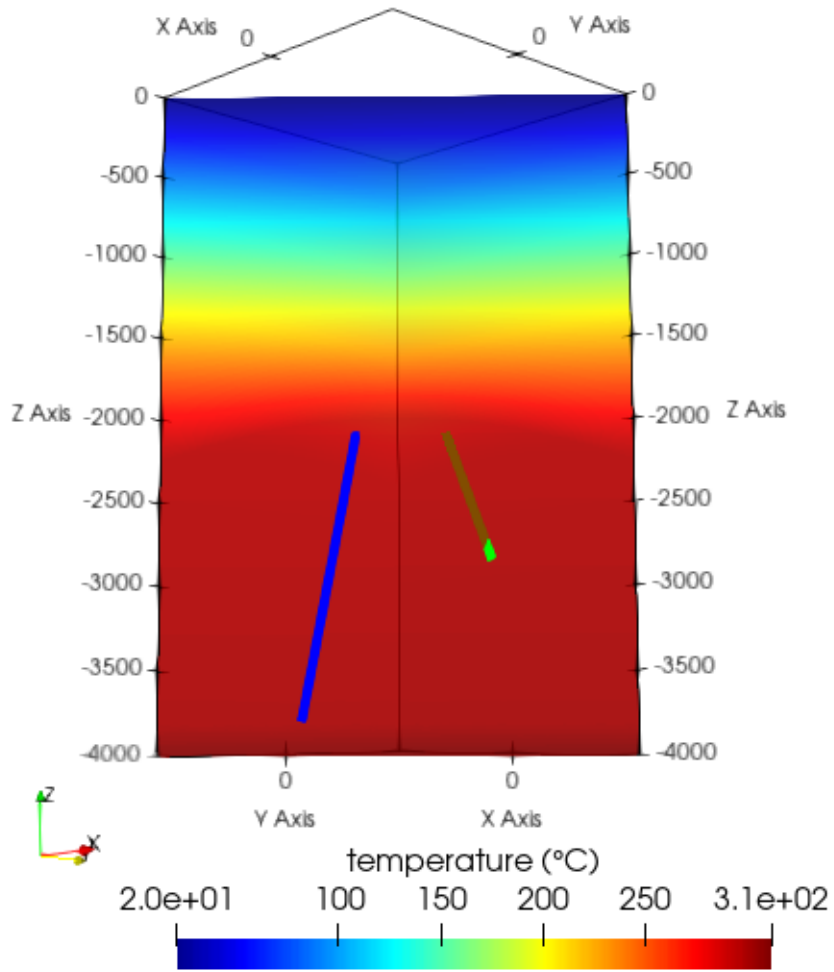


Figure 14: Temperature ($^{\circ}\text{C}$) distribution at the initial state of the steam-dominated reservoir.

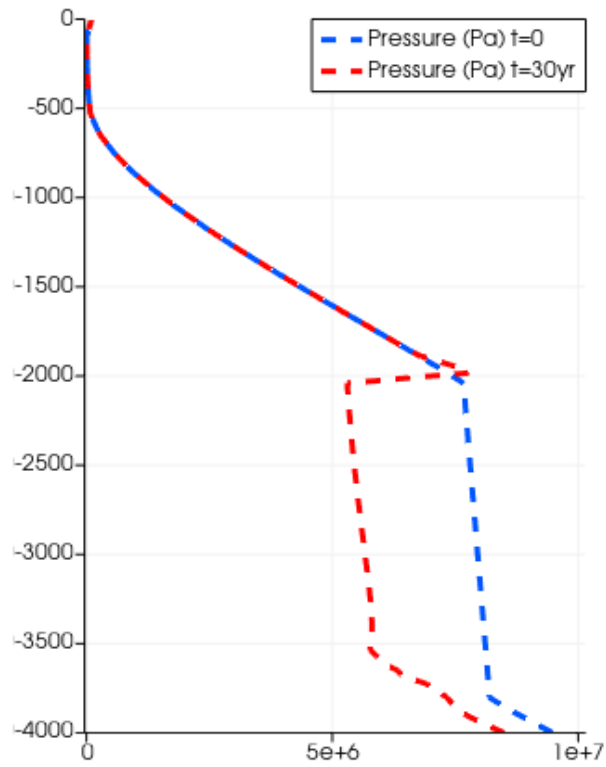


Figure 15: Vertical pressure profiles (passing through the base of the injection well) - blue: initial pressure - red: after 30 years of production

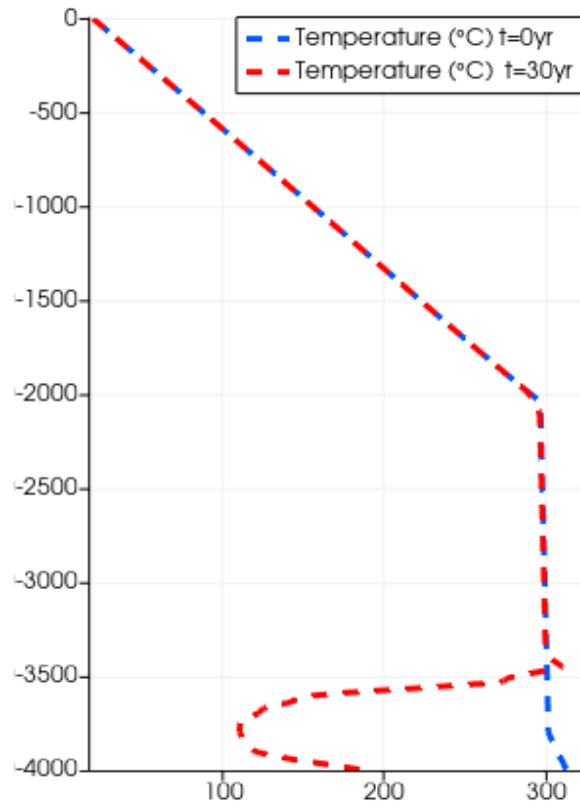


Figure 16: Vertical temperature profiles (passing through the base of the injection well) - blue: initial temperature - red: after 30 years of production.

Geothermal Modeling with ComPASS

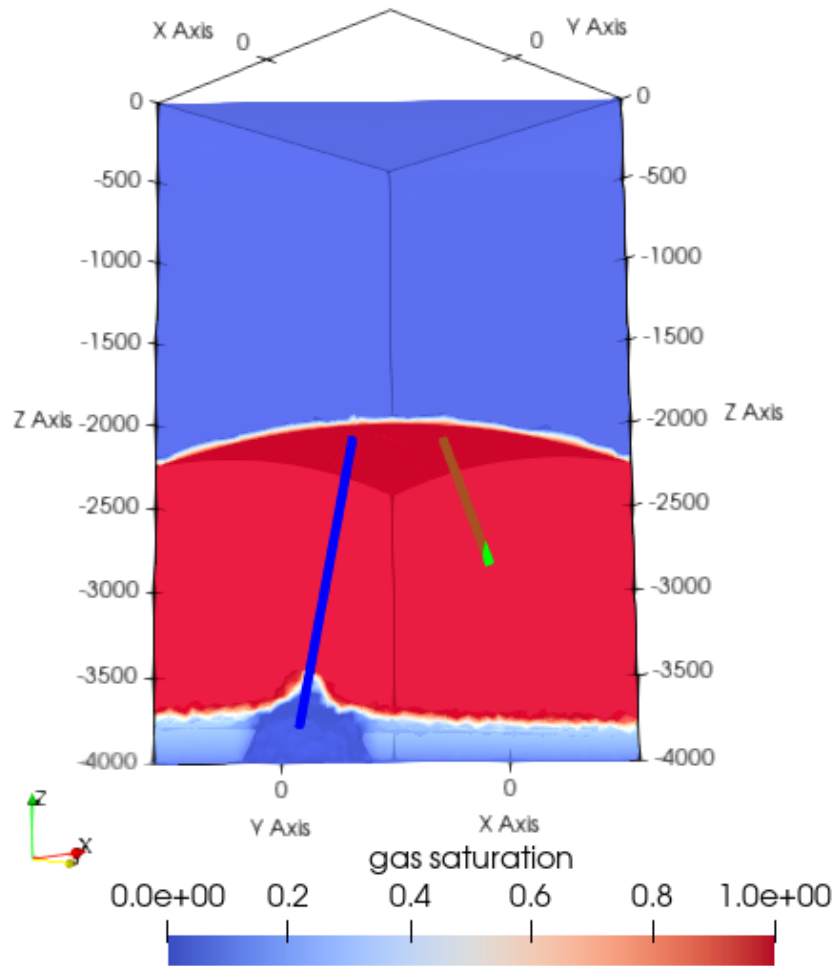


Figure 17: Gas saturation within the reservoir after 30 years of production.

Geothermal Modeling with ComPASS

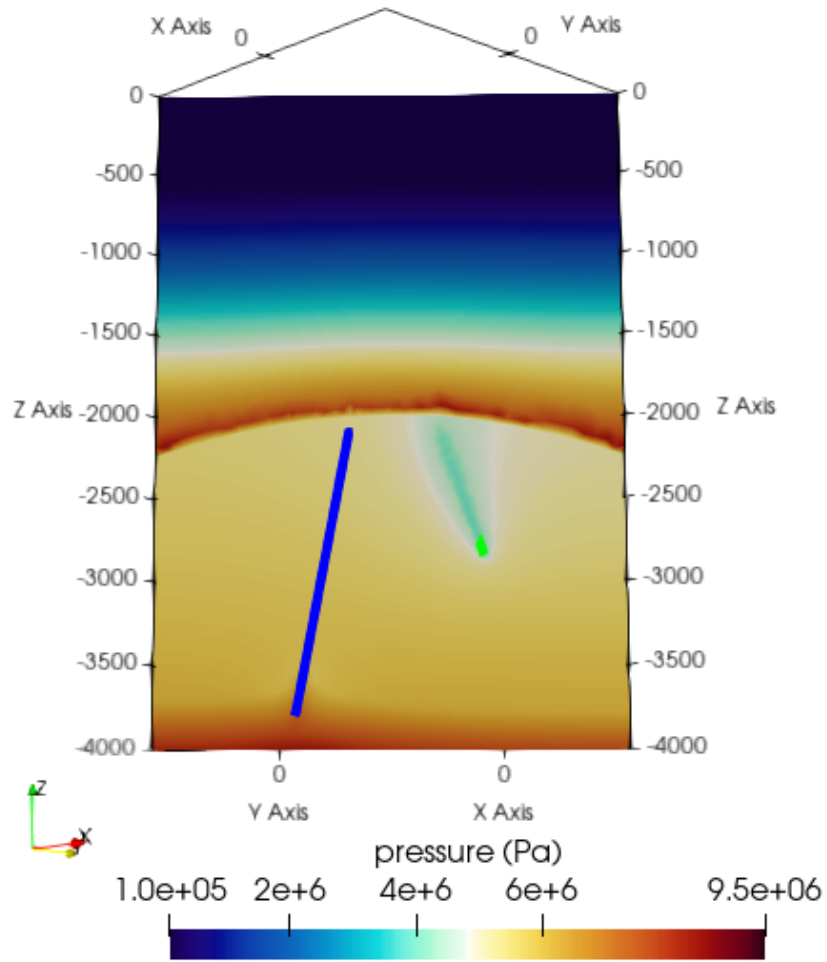


Figure 18: Pressure distribution within the reservoir after 30 years of production.

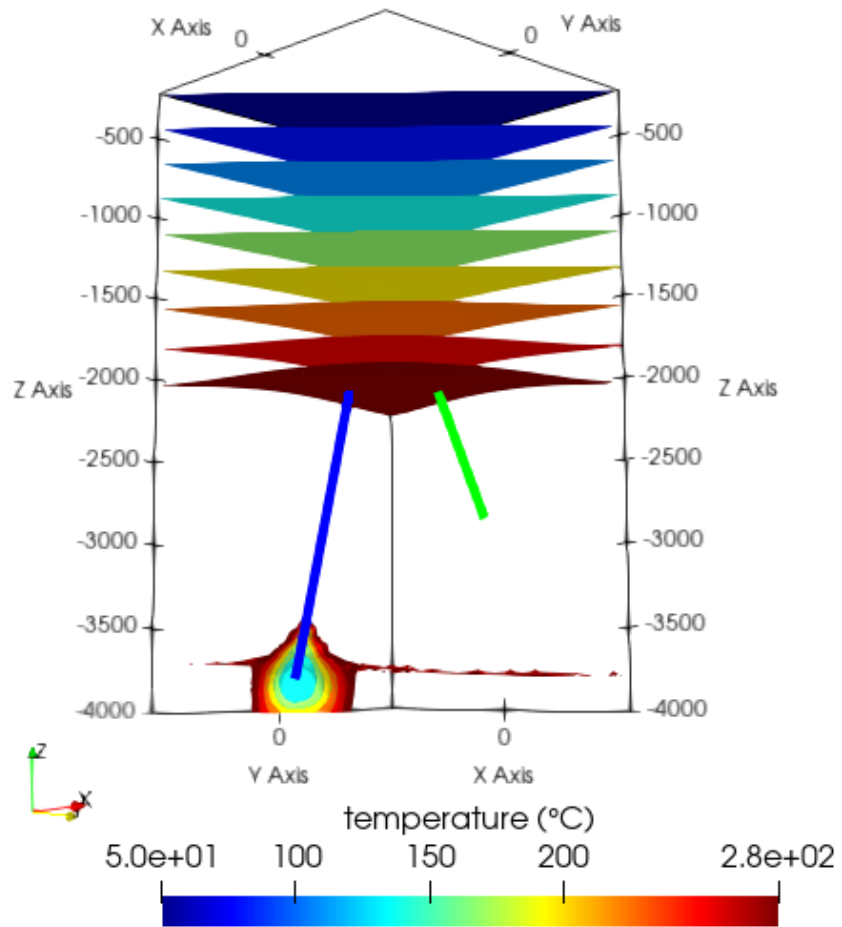


Figure 19: Temperature distribution (°C) within the reservoir after 30 years of production.